Sheltering of sea ice ridges in the ice–ocean drag force: implications from laboratory experiments

S. Wang[1], P. Lu[1], M. Leppäranta [2], Y. Zu[1], Q. Wang[1], Z. Li[1] , P. Hao[1]

[1]State Key Laboratory of Coastal and Offshore Engineering, Dalian University of Technology, Dalian, China.

[2] Institute of Atmosphere and Earth Sciences, University of Helsinki, Helsinki, Finland.

Corresponding author: Peng Lu (lupeng@dlut.edu.cn)

Key points

- **The drag force on the downstream sea ice ridge is reduced significantly and even becomes negative due to the sheltering of the upstream ridge.**
- **The sheltering effect weakens with increasing dimensionless spacing, strengthens with increasing keel angle but isn't related to flow speed.**
- **A new sheltering function has been proposed, providing a reference for the parameterisation of ice-ocean drag coefficient.**

Abstract

The increasing movement and deformation of Arctic sea ice cover results in pronounced drag sheltering effects behind sea ice pressure ridges. This needs to be accounted for in the parameterisation of the form drag of ridges, thereby posing a challenge to evaluate the ice–ocean dynamic feedback. Laboratory experiments were conducted in a water tank to explore the sheltering effect between adjacent ridges of various geometries. The form drag forces on the keel models were measured, and the particle image velocimetry (PIV) system was employed to capture the flow fields surrounding the models to explain the variations in the drag force. The key sheltering parameters were the ratio between keel spacing and keel depth L/H, flow velocity u, and keel slope angle α. The results showed that the drag force F_1 on the upstream keel was close to the value of the single keel case, while the drag force F_2 on the downstream keel was lower, for $L/H \leq 10$ even opposite to the flow direction. Having changed from negative to positive, the sheltering coefficient $\Gamma = F_1/F_2$ increased with increasing L/H. Γ decreased remarkably with steepening α and was independent of u. To fully incorporate the effects of the L/H and α, we propose a new sheltering function fitted with the experimental results: $\Gamma = [1\text{-}1.56\exp(sL/H)]\times 1.20\alpha^{-0.08}$, $s = 0.001\alpha\text{-}0.15$. This function is compared with the previous sheltering functions and

the actual ice conditions in the Arctic Ocean, pointing the way to obtain the final sheltering functions applicable to sea ice dynamics models.

Plain Language Summary

The wake generated by ridge keels in drifting sea ice causes critical sheltering on the downstream ice–ocean interaction, as the keels occupy a significant fraction of the under-ice mixed layer. The flow pattern in the under-ice boundary layer is difficult to measure in situ. Therefore, the sheltering effect was investigated in laboratory experiments, including drag force measurements and flow field mapping with particles. The results revealed that the sheltering effect is sensitive to the keel dimensionless spacing and slope angle but independent of the incoming flow speed. Based on finite depth experiments, a new sheltering function was fitted for the sheltering effect.

1 Introduction

The decline in Arctic sea ice thickness during recent decades has intensified sea ice movement (Kwok et al., 2018; Itkin et al., 2017; Stroeve et al., 2014), leading to the emergence of more deformed ice due to the low strength of thin ice (Itkin et al., 2017; Rampal et al., 2009; Albedyll et al., 2021; Herman, 2011; Leppäranta, 2011). It

53 is anticipated to have a significant impact on sea ice feedback processes, such as ice
54 drift patterns and momentum transfer (Castellani et al., 2014; Armitage et al., 2020;
55 Boutin et al., 2019; Thielen K., 2021; Tschudi et al., 2020). The drag coefficients are
56 critical parameters in these processes, and their modelling has evolved from
57 semiempirical constants to parameterisation schemes associated with sea ice
58 morphology (McPhee, 2008; Leppäranta and Omstedt, 1990; Lu et al., 2011; Brenner
59 et al., 2021; Tsamados et al., 2014). The wind and ocean drag forces are partitioned
60 for the skin friction drag, floe edge form drag, and ridge form drag (Arya, 1975;
61 Garbrech et al., 2002), where the ridge term becomes more important with increasing
62 proportion of deformed sea ice (Tsamados et al., 2014; Brenner et al., 2021; Castellani
63 et al., 2018).

64 A remarkable sheltering effect exists between adjacent ridges due to the wake
65 (Garbrech et al., 1999) that reduces the form drag of downstream ridges. To account
66 for this effect, a sheltering function has been used in drag parameterisation (Lu et al.,
67 2011; Lüpkes et al., 2012; Tasmados et al., 2014). Two forms of sheltering function,
68 viz. exponential and power laws, have been applied: $\Gamma_1 = 1 - \exp(-0.18L/H)$ and
69 $\Gamma_2 = [1-(L/H)^{-0.5}]^2$, where L is the keel spacing and H is the keel depth.

70 The exponential form was originally derived from experiments on terrestrial

forests of varying density and spacing for the decay of downwind speed (Nägeli, 1964). Hanssen-Bauer and Gjessing (1988) applied this function for the first time to calculate drag attenuation in a field of ice floes. It was also utilised in the optimised drag parametrisation considering probability functions of a surface parameter developed by Mai et al. (1996). Lüpkes et al. (2012) adjusted the attenuation parameter from -0.18 to -0.5 based on tunnel observations by Lopez et al. (2005), and they further transformed this into a function of sea ice fraction by assuming a relationship between the spacing and sea ice fraction. However, this simplified scheme works less well at either high or low ice concentration.

Regarding the power law form, Tennekes and Lumley (1972) deduced that the maximum velocity loss behind a cylinder in a turbulent wake is a power function of the distance in a two-dimensional boundary-free plane shear flow. Based on this, Steele et al. (1989) provided a power-law decay function for sheltering between ice floes in a coupled sea ice-ocean model and analysed this sheltering with respect to floes size. Lu et al. (2011) then employed this function in the parameterisation of sea ice–ocean drag coefficient.

Tsamados et al. (2014) used the exponential sheltering function as they considered it to be simultaneously valid for the air-ice and ice-ocean interfaces rather

than the power law. Brenner et al. (2021) compared the ice-ocean drag coefficient calculated from the force-balance using observational data with the parameterisation of Lu et al. (2011) and Tsamados et al. (2014). They showed that the difference of sheltering functions is an important factor affecting the prediction accuracy of the drag parameterisation, opening new ideas for improving the parameterisation schemes. Both exponential and power-law functions have been recognised and cited to date, providing valuable references for subsequent research. However, significant differences exist between land and oceanic boundary layers regarding highly permeable forest and variable sea ice structures (Hanssen-Bauer & Gjessing, 1988). The power function was derived for a cylinder in boundary-free plane flow, while sea ice drifts on the ocean surface, and its accuracy has not been verified by laboratory experiments or numerical simulations. Neither method considers the highly variable structural geometry of ridges. Thus, their applicability for sea ice is worth discussing. Although the wake for structures in tandem configuration has been widely studied in hydrodynamics (Kurtulmuş, 2022; Liu & Chen, 2002; Du et al., 2019; Luo et al., 1999; Rui et al., 2012; Pinarbasi et al., 2015; Kumar & Sen, 2021; Kim et al., 2008; Sohankar, 2012; Lin et al., 2002), no adequate wake functions exist to our knowledge since the studies have mainly focused on small spacings (Du et al., 2019).

It is quite laborious to conduct in situ measurements for the sheltering around ridges, especially due to the harsh conditions beneath sea ice, as opposed to the situation with the atmospheric boundary layer above ice surface (Prinsenberg & Peterson, 2002; Castellani et al., 2014; Garbrech et al., 1999). The depth of ridge keels is 4–5 times the sail height (Timco & Burden, 1997; Kharitonov & Borodkin, 2020; Strub-Klein & Sudom, 2012), and the keel depths are a fraction of 1/5 to 1/2 of the mixed layer depth while the corresponding fraction is usually less than 1/100 in the atmospheric boundary layer (McPhee, 2002). Therefore, the sheltering between keels deserves more attention. A combination of hydrodynamic laboratory experiments and numerical modelling seems to be the best way to address this issue. The former provides the physical truth of flow characteristics at ridges, and the latter extends the experimental results to real ocean conditions (Mortikov, 2016; Pite et al., 1995; Zu et al., 2021).

The goal of the present research was to investigate the sheltering effect between sea ice ridges through a series of water tank experiments, thus providing references for further numerical modelling and keel drag parameterisation schemes. This study is a follow-up to the water tank experiments of Zu et al. (2022) and Wang et al. (2022). Zu et al. (2022) examined the parameterization of the drag coefficient for a single

125 ridge, while Wang et al. (2022) addressed the feasibility of an experimental system to
126 study the sheltering between ridges using a fixed keel shape. Here this experimente
127 has been improved from the preliminary tests and covered more comprehensive
128 factors. This paper is organised as follows: the theory of parameterization on ice-
129 ocean drag coefficient is briefly summarized in Section 2 as a background. And in
130 Section 3, the experimental setup is introduced, including the force and flow field
131 measurement system. The dependence of the drag force and sheltering effect on the
132 flow velocity, dimensionless spacing, and keel slope angle are investigated in Section
133 4. Section 5 discusses the sheltering in finite water depth, the impact of sheltering
134 function on ice-ocean drag coefficient and sea ice motion, and limitations in the
135 laboratory experiment. Finally, conclusions are drawn in Section 6.

136 **2 Theory of ice-ocean drag coefficient parameterization**

137 Ice-ocean shear stress τ_{io} is commonly described by the quadratic drag law:

138 $$\tau_{io} = \rho C_{io}(\boldsymbol{u}_i - \boldsymbol{u}_o)|\, \boldsymbol{u}_i - \boldsymbol{u}_o \,| \quad (1)$$

139 where ρ is seawater density, C_{io} is the ice-ocean drag coefficient, $\boldsymbol{u}_i$ is the drift velocity
140 of ice and $\boldsymbol{u}_o$ is ocean current velocity at the reference depth. Based on the drag
141 partition theory, the total ice-ocean drag force is given as the sum of the form drags of

142 the floe edge and ridge keel, and the skin friction drag (Arya, 1975). Accordingly, the
143 total ice-ocean drag coefficient C_{io} in sea ice geometry-based parameterisation
144 schemes can be calculated as follows (Lu et al.,2011; Tsamados et al., 2014):

145 $$C_{io} = C_r + C_f + C_s \tag{2}$$

146 $$C_r = \frac{1}{2} c_r A \frac{H}{L} \Gamma\left(\frac{L}{H}\right) P_{r0} \tag{2a}$$

147 $$C_f = \frac{1}{2} c_f A \frac{d}{L_f} \Gamma\left(\frac{d}{L_f}\right) P_{f0} \tag{2b}$$

148 $$C_s = c_s A\left(1 - m \frac{H}{L}\right), \frac{H}{L} \le \frac{1}{m} \tag{2c}$$

149 where C_r, C_f, and C_s represent ridge keel drag coefficient, floe edge drag coefficient,
150 and skin drag coefficient, respectively, c_r , c_f and c_s are the corresponding local drag
151 coefficients, A is the sea ice concentration, H is keel depth, L is keel spacing, and d/L_f
152 is the ratio of the floe draft to floe length. The ratio H/L is the ridging intensity, and
153 AH/L equals the sum of keel depths per unit length. In Eq. (2a, b) P_{r0} and P_{f0} are
154 boundary layer integration functions, with some differences due to the choice of $\boldsymbol{u}_o$.
155 Tsamados et al. (2014) set $\boldsymbol{u}_o$ equal to the velocity associated with the inner boundary
156 layer which obeys the logarithmic distribution law, $P_{r0} = P_{f0} = [\ln(h_{ref}/z_0)/ \ln(z_{ref}/z_0)]^2$,
157 where z_0 is the roughness length and the selection of h_{ref} and z_{ref} is referred to
158 Tsamados et al. (2014). $P_{r0} = P_{f0} = 1$ when $\boldsymbol{u}_o$ was selected as the undisturbed far-field
159 flow velocity by Lu et al. (2011). These two parameterisations of Eq. 2a using

different boundary layer functions can be converted, with a transformation factor of 0.76 proposed by Zu et al. (2022). In Eq. (2c), m is skin drag attenuation parameter. In Eq. (2a, b), $\Gamma=\Gamma(L/H)$ is the empirical sheltering functions mentioned above. The same sheltering function is employed between adjacent ice floes (Eq. 2b) and between adjacent ice ridges (Eq. 2a). We only focus on the sheltering function in ridge keel drag in this study.

3 Methods

3.1 Experimental setup

The laboratory experiment was conducted in a water tank which was 11.5 m long, 0.45 m wide, and 0.50 m deep (Fig. 1a). The basic experimental setup was originated by Wang et al. (2022) but has been improved here as summarized below. Similarity treatment was adopted for the major parameters based on dimensional analysis. The dependent quantities were the drag force F, keel spacing L, keel depth H, water depth D, flow velocity u, keel slope angle α, fluid density ρ, and kinematic viscosity coefficient of fluid v. H, ρ, and u were selected as the fundamental dimensional quantities, and the derived dimensionless quantities were (Table 1): $\pi_1 = c_r$ is the local drag coefficient, π_2 is the dimensionless spacing, π_3 is Reynolds number (Re),

177 and π_4 is dimensionless depth. It is necessary to ensure that the ranges of these
178 dimensionless quantities in the water tank experiment are consistent with the natural
179 conditions.

180 Table 1 Similarity basis of the model experiment

Dimensionless quantities	π_1	π_2	π_3	π_4	π_5
Expression	$\frac{F}{\rho u^2 H}$	$\frac{L}{H}$	$\frac{uH}{v}$	$\frac{D}{H}$	α

181

182 The keel model was set up as a solid isosceles triangle, which has been used in
183 many laboratory experiments (e.g., Pite et al., 1995; Zu et al., 2021) and geophysical
184 applications (Roberts et al., 2019; Lemieux et al., 2015). The model material was
185 plexiglass, as used by Waters and Bruno (1995), Pite et al. (1995), and Zu et al. (2021).
186 The model shape corresponds to observed sea ice ridge keels (Timco & Burden, 1997),
187 but the macroporosity of 11-20% between keel blocks (Kharitonov & Borodkin, 2020;
188 Strub-Klein & Sudom, 2012) was ignored. A low macroporosity may occur in nature
189 near the waterline due to ridge consolidation (Leppäranta et al., 1995; Roberts et al.,
190 2019). The keel slope angle of first-year ice is mostly in the range of 20°-50°, with a
191 mean value of 29.6° (Strub-Klein & Sudom, 2012; Timco & Burden, 1997; Davis &

192 Wadhams, 1995) and a maximum of 87° (Kharitonov & Borodkin, 2020). The keel
193 depth (minus background ice thickness) mostly varies from 2 to 12 m, with an average
194 of 5 m and maximum exceeding 27 m, (Metzger et al., 2021, Kharitonov & Borodkin,
195 2020; Wadhams et al., 2011).

196 The parameter settings for the experiment are given in Table 2. All four keel
197 depths H were measured with the fixed tank depth D = 0.45 m, thus D/H = 3.75–22.5,
198 whereas the variable water depth experiments were conducted with α = 45°, H = 0.12
199 m, and D = 0.30 - 0.50 m. For the keel model H = 0.02 m, the lowest flow velocity is
200 u = 0.2 m/s since the drag force is too small (down to 10^{-2} N) to be accurate for u = 0.1
201 m/s. The model for α = 90° was a 5 mm thick rectangular slice.

202 The dimensionless spacing L/H is a classical parameter in wake analysis (Du et
203 al., 2019), and it is equal to the inverse ridging intensity, which is a common spatial
204 statistic of ridging (see Leppäranta, 2011). It was ensured that the keel models of
205 different depths corresponded to fixed L/H. The min and max L/H achievable for
206 different keel sizes depend on the width of the model and the length of the tank: L_{min} =
207 $2(H+0.02)/\tan(\alpha)$, where 0.02 m was freeboard, and L_{max} = 6 m in the stable uniform
208 flow section, accounting for the length of the tank and the locations of the inlet and
209 outlet. The characteristic length in the Reynolds number was chosen as the wetted

perimeter length of the keel model, $Re = [2uH/\sin(\alpha)]/\upsilon$, $\upsilon = 1.003\times10^{-6}$ m^2/s. The range of Re was 8×10^3 to 2.47×10^5. The laboratory experiments were considered similar to the natural marine environment when the flow was turbulent or $Re > 10^4$ (Zu et al., 2021). The cases of $Re < 10^4$ were at the margin and may occur in nature at near stationary ice conditions.

Table 2 Experimental cases for the drag force measurement. The asterisk shows the cases the flow field was measured by the PIV system.

Drag force measurement	
u (m/s)	0.1, 0.2,0.25*,0.3*,0.35
H (m)	0.02*,0.04*,0.08*,0.12*
α (°)	20*,30,45*,60*,90
L/H [Note1]	2.5*, 5*, 7.5*, 10*, 20*, 30, 50,70,100
D (m) [Note2]	0.50,0.45*,0.40,0.35,0.30

3.2 Drag force measurements

The drag force measurement device is shown in Fig. 1b. The selected speed was obtained by adjusting the frequency of the flow generator machine, which is linearly related to the speed. A flow stabiliser was added to the inlet of the tank to ensure a uniform inflow. Three brackets were placed on the side rails of the tank, and they

were used to connect the acoustic Doppler velocimeter (ADV), the upstream and downstream keel models, abbreviated as keel-1 and keel-2, respectively.

Real-time monitoring and recording of the incoming flow velocity was conducted using the ADV. The force sensors were fixed to the keel models vertically and connected to the screw on the bracket integrally, enabling height adjustment. Two-component force sensors were chosen to measure the form drag force in the flow direction, with a range of 10 N. To reduce errors in the data, the spacing of the keels was adjusted by only moving keel-2. In addition, a round rod (6 mm diameter) was fixed to keel-1 bracket as a nonload item (Fig. 1b). Its original goal was to record the vibration of the flow generator and the brackets above the tank that helped to remove the disturbances on the measurements of keel drag force. This was similar with the experiments used to record the noise of cylinders with a large aspect ratio in a wind field (Reza et al., 2023). We verified that the effect of disturbances such as flow generators was extremely small (<0.9%) and could be ignored. Altogether, 730 groups of force measurement data were obtained (Table 2).

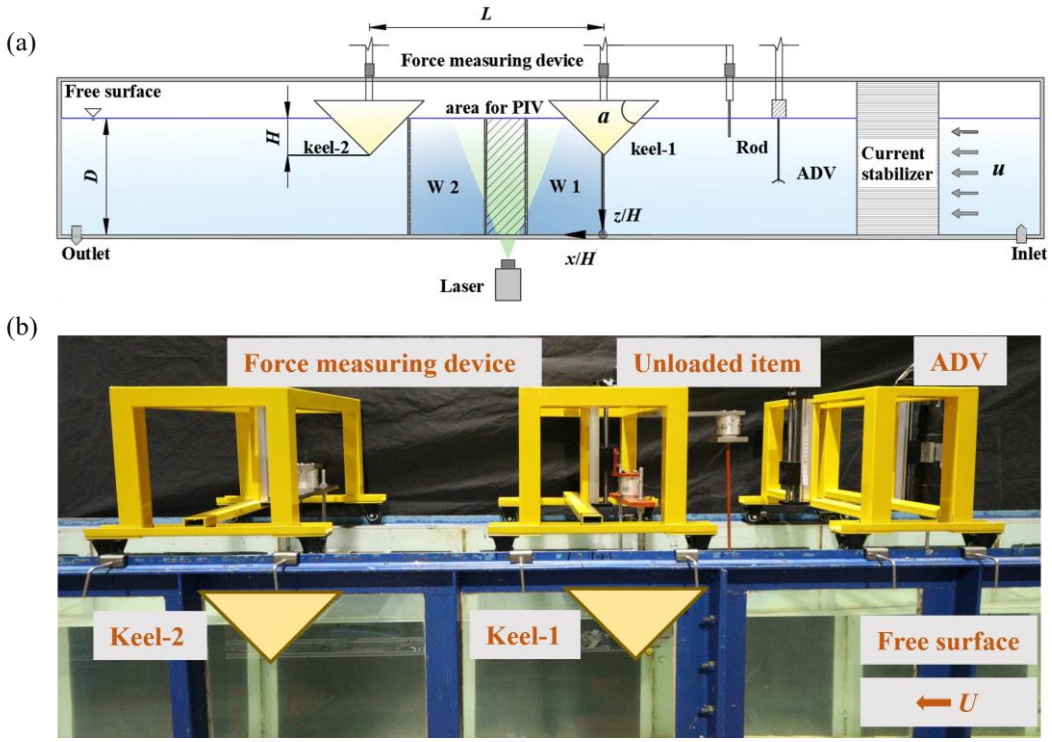

Fig. 1 (a) A schematic drawing of the study tank. W1 and W2 represent the windows of the PIV shots, and the shaded area in the middle is the overlap. (b) A photograph showing the model test device.

3.3 Flow field measurement

Particle image velocimetry (PIV) is an instantaneous, multipoint, noncontact hydrodynamic measurement method that can record velocity distributions over many spatial points in the same transect, providing a rich spatial structure of the flow field (Westerweel et al., 2013). The PIV system was used in some groups in the experiments (Table 2) with the shooting positions (windows 1 and 2) shown in Fig. 1(a). The origin of the coordinate system was located at the intersection of the midline

249 of keel-1 and the free surface, and the positive axis directions are shown by the arrows
250 in the fig.1(a).

251 The PIV installation diagram is depicted in Fig. 2(a). The steps of the PIV
252 method were as follows: First, to eliminate the excess light in the environment,
253 darkroom conditions were created, and the test area was shielded. The tracer particles
254 added to the fluid were hollow glass beads with a diameter of 50 μm and a density of
255 1.05 g/cm^3, and with excellent light reflectivity and high followability. A continuous
256 laser with a wavelength of 532 nm was used as the light source to illuminate the area
257 of interest. A black coating was added to the model to reduce its surface reflection and
258 the edge effect. Finally, the Photron FastCAM SA5 ultrahigh-speed camera was used
259 to take continuous images at a fixed position in the given time interval, with a
260 resolution of 1024 × 1024 pixels (Fig. 2b). It can be adjusted in both the horizontal
261 and vertical directions, ensuring that the camera is perpendicular to the laser surface
262 when capturing.

263 The Window 1 and Window 2 were both of approximately 45 × 45 cm size. The
264 overlapping areas of the windows were averaged and then spliced together. The
265 captured frame rate was 250FPS and the storage time for the cases was 60s. An
266 interrogation window of 32 × 32 pixels was used to capture a sort of high

displacement, and then 16 × 16 pixels were taken in the final pass to give a refined vector resolution (Xue et al., 2023). The maximum pixel displacement in the PIV image was 5.47 pixels at u= 0.25 m/s. Considering the systematic error of 2D PIV, the window deformation, and the error from speed control, the relative uncertainty was 4-5% (Singha et al., 2009; Jin et al., 2014), equivalent to 0.22-0.27 pixels.

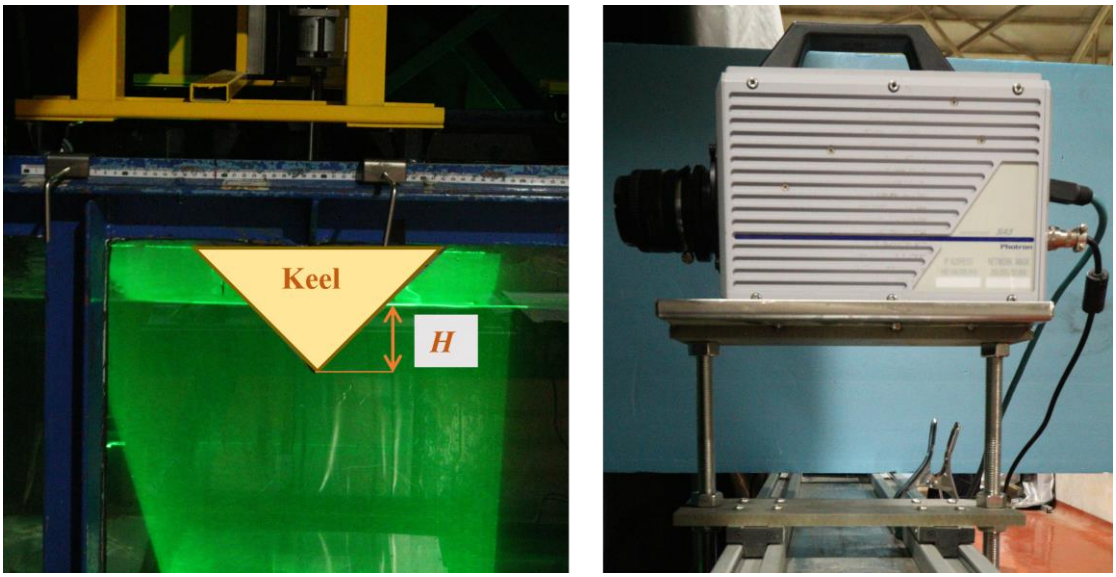

Fig. 2 (a) PIV experimental installation diagram; (b) Camera arrangement diagram

4 Results

4.1 Drag force on ice ridges

Fig. 3 shows the drag forces on the upstream and downstream keels vs. L/H for α

279 = 45° and H = 0.08 m. The other cases are not shown because of the similar patterns.
280 Fig. 3(a) shows that L/H influences F_1 only within L/H <10, where F_1 increased by 5%
281 due to the presence of keel-2. Thus, the upstream keel drag is the same as in the case
282 of an individual keel which has been investigated thoroughly by Wu (2016) and
283 provides a reference for the decay of the downstream drag F_2. Fig. 3(b) reveals that F_2
284 was reduced as a result of sheltering by the upstream keel, and this attenuation
285 decreased with increasing L/H as F_2 gradually approached F_1 as described in more
286 detail in Section 3.4.

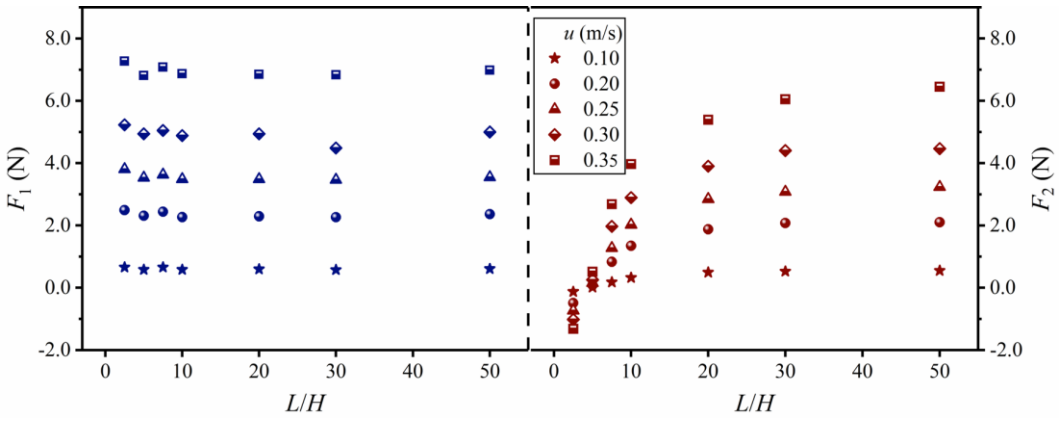

287

288 Fig. 3 (a) The drag force F_1 and (b) the drag force F_2 vs. the L/H for α = 45° and H =
289 0.08 m.
290
291 The drag force $F_2 = F_2(u^2)$ for α = 45° and H = 0.08 m is shown in Fig. 4. The
292 dependence was linear, consistent with the classical drag force formula (Tennekes &

293 Lumley, 1972; Arya, 1975; Wamser & Martinson, 1993). F_2 appeared negative at L/H
294 $\leq$ 5, when keel-2 was located in the recirculation zone formed by flow separation
295 behind keel-1. This reverse drag force was also linear with u^2. The presence of
296 different ranges of recirculation zones has been demonstrated in submerged wake
297 experiments for a conical island (Oruo et al., 2017) and in tank experiments with
298 rectangular columns placed in series (Pinarbasi et al., 2015).

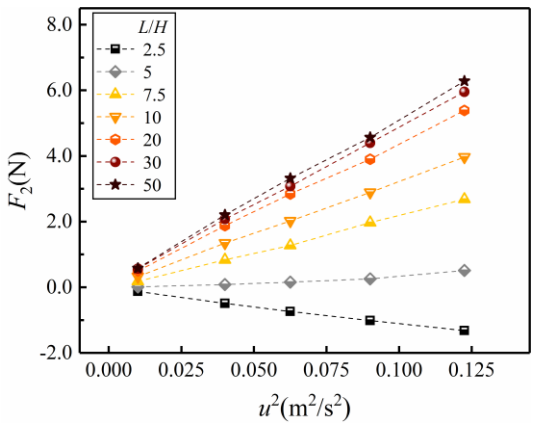

299

300 Fig. 4 The drag forces F_2 vs. the velocity squared u^2 when α = 45° and H = 0.08 m

301

302 In the mechanism of drag variation, the main turbulent structures and the
303 development in the wake field around keels are essential. The time-averaged
304 streamlines and dimensionless velocity $\bar{u}/u_0$ for α = 45°, u_0 = 0.25 m/s, and L/H = 5 (H
305 = 0.08 m) are plotted in Fig. S1, corresponding to F_1 = 1.94 N and F_2 = -0.06 N. The
306 characteristic structures in the wake mainly included recirculation zones, vortex

shedding, separated shear layers and an acceleration zone (Ouro et al., 2017), analysed in Text S1. The development of turbulent structure leads to changes in the pressure difference between the leading and lee edges of the keel-2, which is the essence of the drag force.

4.2 Influence of flow velocity on the sheltering effect

The ratio of the drag forces $\Gamma = F_2/F_1$ is defined as the sheltering coefficient, which characterises the strength of the sheltering between the keels. Fig. 5 shows this coefficient as a function of the squared flow velocity for α = 45° and H = 0.12 m. As u^2 increased, Γ remained stable within 4.2%. According to the dimensional analysis in Table 1, the flow velocity u impacted the sheltering effect by changing only Re, which is crucial in the laminar flow regime but barely affects the turbulent regime (Zu et al., 2021). Since the ocean currents under sea ice are mostly turbulent (McPhee, 2008; Kharitonov & Borodkin, 2020), Γ is independent of the u. Based on the quadratic drag laws, $\Gamma = F_2/F_1 \sim u_2^2/u_1^2$ = constant at a fixed L/H, where u_1 and u_2 are the flow velocities at keel-1 and keel-2, respectively. Thus, u_2/u_1 depends only on L/H for the fixed α = 45°, implying that the velocity deficit caused by keel was not connected with the incoming flow. Li and Sherman (2015), in a study focused on the

aerodynamics and morphodynamics of the sheltering effect behind also confirmed that the ratio of the disturbed velocity to the incoming velocity at a certain elevation and distance was nearly an independent factor.

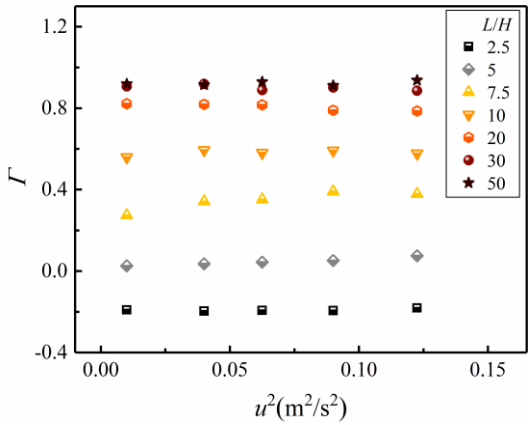

Fig. 5 The sheltering coefficient Γ vs. the squared velocity u^2 for α = 45° and H = 0.12 m

4.3 Influence of the ridge spacing on the sheltering effect

Γ as a function of the L/H for α = 45° is shown in Fig. 6. The error bars show the standard deviation of different sizes of keels. An exponential function was chosen to fit in the data (R^2 =0.99), whose form was similar with the sheltering function of Hanssen-Bauer and Gjessing (1988). Based on the growth and asymptotic behaviour, the function was divided into two parts in the analysis, for L/H <30 and $L/H \geq 30$.

At $L/H < 30$, keel-2 drag was subject to strong attenuation from the wake of keel-

1. The sheltering coefficient was negative and changed sign at approximately L/H = 5, a similar critical value of L/d=5 was found for the drag on the downstream cylinder (diameter d) in simulations with two cylinders in tandem by Li et al. (2018). An examination of the flow pattern was needed to interpret the phenomenon. For L/H > 5, sheltering gradually became weaker.

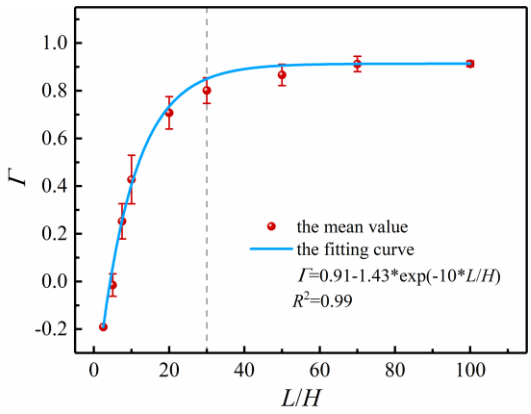

Fig. 6 The sheltering coefficient Γ vs. dimensionless spacing L/H when α = 45°. The blue curve represents the fit for $\Gamma = \Gamma(L/H)$. The dashed line at L/H=30 separated the growth and asymptotic parts of the curve.

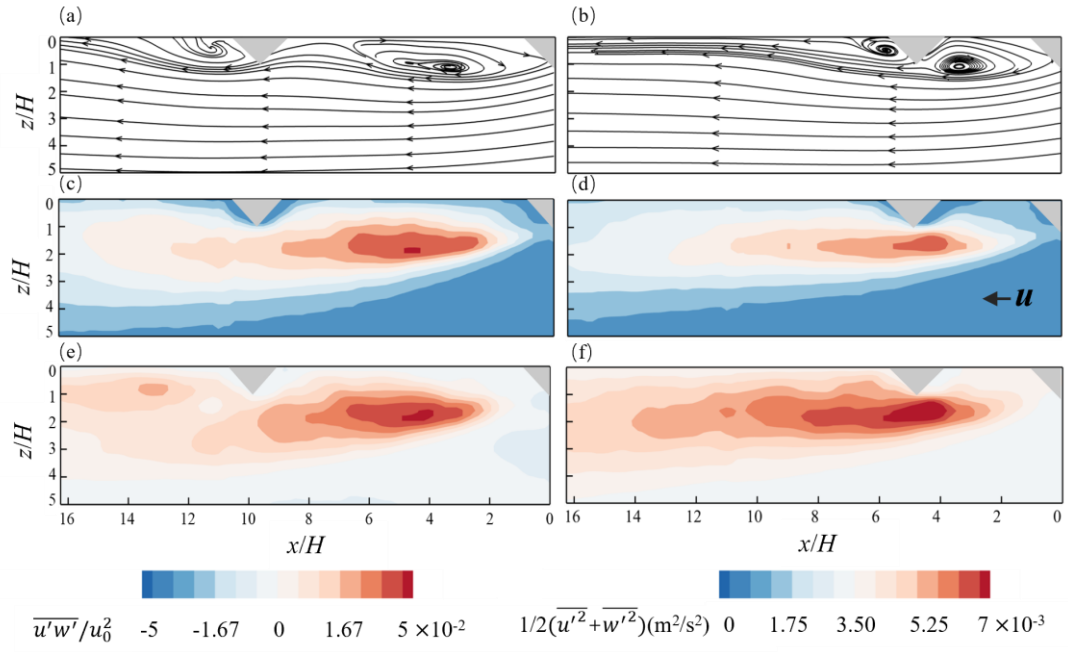

Fig. 7. Contours of time-average streamlines (a, b), turbulent kinetic energy 1/2($\overline{u'^2}$+$\overline{w'^2}$) (c, d), and dimensionless Reynolds shear stress ($\overline{u'w'}/u_0^2$) (e, f). L/H=5 (b, d, f) and L/H=10 (H=0.04 m) (a, c, e). α = 45°, u_0=0.25 m/s, and u' and $w'$are the velocity fluctuations along the flow and vertical directions, respectively.

Fig. 7 shows the streamlines, turbulent kinetic energy (TKE), and dimensionless Reynolds shear stress for L/H=5 and L/H=10, α = 45°, corresponding to Γ = -0.07 and 0.34, respectively. Reducing the spacing between the keels led to an increased local blockage that induced more complex flow patterns. As L/H increases, the mixing wake around the keels will exhibit three major regimes (Kurtulmuş, 2022; Sakamoto et al., 1987; Sohankar, 2012). Two are shown here, with differences in the dominant

359 turbulence structure and development mechanism of the wake as the fundamental
360 reason for the drag variation.

361 When the two keels are very close (Fig. 7b, d, f), the shear layer separated by
362 keel-1 will adhere to the surface of keel-2 where the vortex wraps around, so they can
363 be treated as one bluff body (Du et al., 2019). This flow pattern is denoted as a single
364 slender-body regime (Sohankar, 2012), which exposed the leading face of keel-2 to a
365 strong suction and resulted in a thrust (negative F_2) rather than a drag force with $\Gamma < 0$
366 for L/H=5. The peak values of TKE and Reynolds stress occurred underneath keel-2
367 along the transition from the recirculation region to the far wake, corresponding to the
368 region where shear-layer vortices lost coherence due to interactions with the incoming
369 flow and backflow. The continuous vortex structure was gradually shed. The Reynolds
370 stress was consistently higher up to x/H=14, which meant a long section of intensive
371 turbulent momentum exchange. Thereafter, the stress gradually dissipated downwards
372 in the direction of the flow.

373 Figs. 7a, c, e show the reattached flow regime (Sohankar, 2012), characterised by
374 synchronised vortex shedding from each cylinder. The separated shear layer at keel-1
375 found sufficient space to develop and roll into the distance between two keels, with
376 the reattachment positioned in front of keel-2 (x/H = 6-8). Hence, secondary

separation occurred at the tip of keel-2 which presents a co-shedding vortex flow regime (Kurtulmuş, 2022; Sohankar, 2012). The vortex length became distant with the first flow separation reattaching at x/H = 7, while the second reattachment point was shifted to x/H = 14. The locations of the peak values of TKE and Reynolds stress were advanced to x/H = 2-4 between keels, accompanied by the enhancement of the TKE and the weakening of the Reynolds stress which was elevated at the intersection of eddies and incoming flows behind keel-2 due to the induced secondary separation, but it was weaker. The reduction in the turbulence intensity in the wake also indicated a decrease in the sheltering capacity of the wake.

In the range of $L/H \geq 30$, Γ increased with L/H towards the asymptote, and the wake field was gradually restored to an undisturbed state. The third mode, appearing in this far-wake region, manifested as vortices falling off independently of the two structures. In the aerodynamic experiments by Sakamoto et al. (1987) on two square prisms in tandem, this wake mode occurred when $L/H > 27$.

4.4 Influence of the keel slope angle on the sheltering effect

Fig. 8 shows Γ against α, with the error bars representing the standard deviation. Since negative values of Γ occurred, the logarithmic coordinate transformation was

performed for Γ+0.5. With increasing slope, the sheltering coefficient tended to decrease. Linear fits in the plot were excellent (R^2=0.98), implying a power function relationship Γ+0.5 = 3.02*$\alpha^{-0.31}$ (20° ≤ α ≤ 90°). The decline in Γ was strong at α = 20°–30°, which is the common range of the slope Arctic sea-ice ridges (Timco & Burden, 1997; Strub-Klein & Sudom, 2012). Furthermore, the decrease of Γ caused by the increasing α revealed different characteristics in the regimes L/H < 20 and L/H ≥ 20, represented in red and blue colours, respectively. The wake can be divided into near and far wake zones (Vermeer et al., 2003; Williamson, 1996), and the influence of the keel shape on the wake field was mainly concentrated in the near-wake region, while the geometry was no longer important in the far-wake region. For instance, when α increased from 20° to 90°, Γ decreased from 0.65 to 0.22 at L/H = 10 and from 0.93 to 0.78 at L/H = 50.

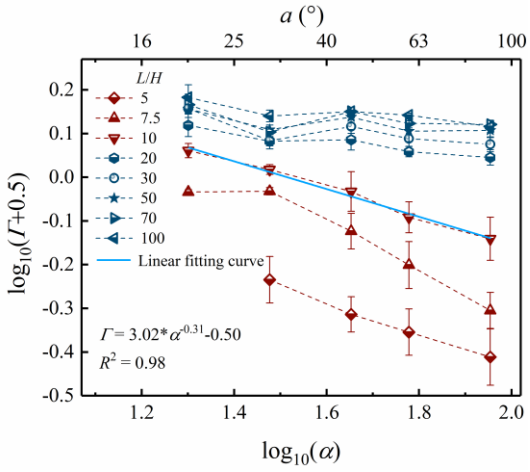

Fig. 8 The sheltering coefficient Γ vs. slope angle α. The dashed red curves represent

408 the near-wake region, the dashed dark blue curves represent the far-wake region, and
409 the solid blue line represents the fitted curve for L/H =10.
410
411 More insight into the flow characteristics in the near-wake region could be
412 obtained by extracting the PIV flow field results at different slopes. Fig. 9 illustrates
413 the time-average streamlines, TKE, and Reynolds shear stress for α = 20° and α = 60°
414 when L/H=10, corresponding to Γ = 0.65 and 0.31. The result can be analysed in
415 conjunction with the flow field at α = 45° and L/H=10 in Fig. 7(a, c, e). The wake
416 flow extent at α = 20° had a small longitudinal range of z/H = 1-1.5, and the
417 secondary separation was weak near keel-2, with no significant vortex production
418 behind (Fig. 9a). The attachment point was at x/H = 5-6. The flow separation at keel-1
419 with α = 60° was more intense (Fig. 9b), and the reattachment point was shifted to x/H
420 = 7-8, implying a deferred shedding process of the vortex. Steeper angles lead to
421 increased pressure gradients around the keel, which affect the flow separation process
422 and the vortices that roll up behind the keel, resulting in different sized vortex
423 structures, vortex shedding patterns, and dissipation (Wang et al., 2017).
424 Overall, the wake generated with α = 60° produced stronger turbulence intensity
425 and more active flow separation processes compared to α = 20° and α = 45°, leading

to an increase in sheltering strength and extent. The larger range of TKE and Reynolds stress peak values was maintained up to x/H = 7-8 and z/H = 3-4. The increase in the Reynolds stress enhanced the momentum transfer across the shear layer, thereby delaying wake recovery. The first triggered peak value occurred at x/H = 2-4, developing and dissipating along the flow direction. The Reynolds stress peaked again but at a significantly lower level than in the first one due to the secondary disturbance of keel-2 that was also related to α. The Reynolds stresses behind keel-2 were higher with α = 60° than with 45° and 20° due to the larger velocity gradient of the fluid flowing through the keel. The greater shear stress intensifies the level of turbulence in the wake, accompanied by a significant increase in TKE.

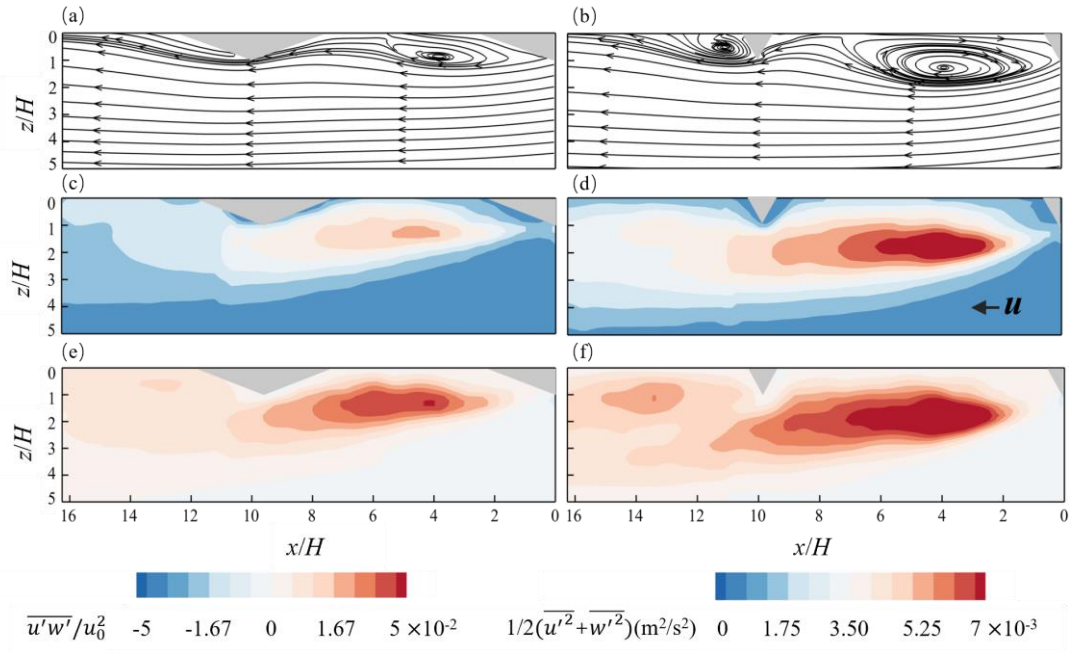

Fig. 9 Contours of time-average streamline (a, b), turbulent kinetic energy $1/2\left(\overline{u'^2}+\overline{w'^2}\right)$ (c, d), and Reynolds shear stress $\overline{u'w'}/u_0^2$ (e, f) for α = 20° (a, c, e) and α = 60° (b, d, f) when L/H = 10, corresponding to Γ = 0.65 and 0.31, respectively.

5 Discussion

5.1 Sheltering functions

The sheltering function was affected not only by the dimensionless spacing L/H but also by the slope angle α, but it was independent of the flow velocity u. In Sections 4.2-4.4, the curve $\Gamma = \Gamma(L/H)$ at α=45° was better fitted by the exponential function (Fig. 6), similar with the previously presented sheltering function. The relationship between Γ and α was given by a power law (Fig. 8). To obtain a new expression of the sheltering function based on the present experimental data, the two functional forms above are combined. The least squares method was used for the optimal solutions of the pending parameters. The resulting sheltering function $\Gamma = \Gamma(L/H, \alpha)$ is:

$$\Gamma = [1\text{-}1.56\exp(sL/H)]\times 1.2\alpha^{-0.08}\ ,\quad s = 0.001\alpha\text{-}0.15 \tag{3}$$

The range of application is $2 \le L/H \le 110$ and $10° \le \alpha \le 90°$. Formerly s was a

455 constant s = -0.18 (Hanssen-Bauer & Gjessing, 1988) and s = -0.5 (Lüpkes et al.,
456 2012), but here it was found that s increased with α. To account for this, s was taken
457 as a linear function of α. The exponential factor reflects the influence of both
458 arguments, while the power function factor depends only on the slope angle. First, the
459 exponent sL/H determines the sign of the sheltering coefficient. At sL/H = -0.44, we
460 have Γ = 0 and s = -0.14 when α =10° and -0.06 when α =90°. The minimum and
461 maximum values of sL/H were -16.8 and -0.12, respectively; Γ >0 when -16.8< sL/H
462 < -0.44, while Γ <0 when -0.44< sL/H < -0.12. In the limiting cases, when $L\rightarrow 0$,
463 $\Gamma \rightarrow -0.672\alpha^{-0.08}$, and when $L\rightarrow$ infinity, $\Gamma \rightarrow 1.20\alpha^{-0.08}$. Ninety percent of the increase
464 in Γ with increasing L was concentrated at $L/H \leq 30$. In this range, the reduction in Γ
465 could reach 69% due to the steepening of the keel slope. Fig. 10 shows the fitted
466 curves (Eq. 3) for α =20°, 45° and 60° within $2 \leq L/H \leq 110$, with R^2 = 0.97, RMSE
467 =0.07.

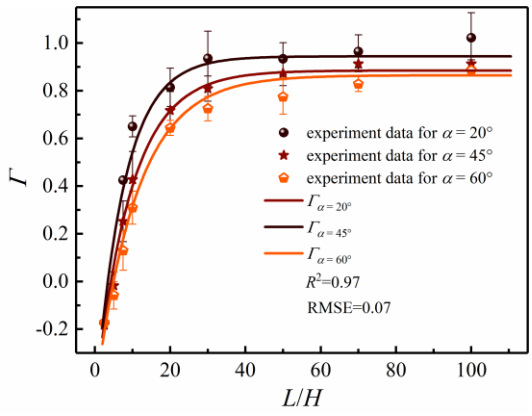

468

Fig. 10 Comparison of Eq. (3) with the experimental data. The adjusted R^2 is 0.97, and the root mean square error is 0.0697. The solid points are the experimental results, and the error bars represent the standard deviations.

Fig. 11 compares our formula (Eq. 3) with the two previously reported equations. The pink shaded area presents Eq. (3), extended through α = 10°-90°. The average slope angles in different papers varies, but they are generally about 30° which was chosen here as the representative angle (Timco & Burden, 1997; Strub-Klein & Sudom, 2012). Eq. (3) was then $\Gamma_{30} = 0.92\text{-}1.44 \exp(-0.12L/H)$. The factor -0.12 in the exponent is larger than the fixed constant -0.18 (Hanssen-Bauer & Gjessing, 1988) and -0.5 (Lüpkes et al., 2012). The minimum value of this factor in Eq. (3) was -0.14, and thus Eq. (3) represents stronger sheltering than the exponential function Γ_1 but weaker than the power function in Γ_2. Compared to Γ_{30}, the exponential function was 15.2% higher, while the power function was 17.1% lower within L/H=2.5-100. Eq. (3) includes the reverse drag force at small spacings and the effect of the keel slope.

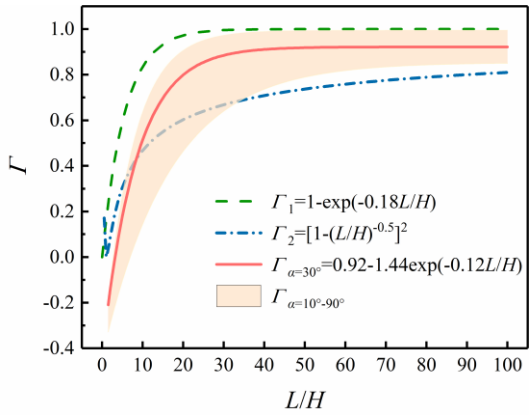

Fig. 11 Comparison between Eq. (3) (the pink shaded for α = 10° - 90°) and the previously reported exponential (green dashes) and power (blue dotted lines) functions. α = 30° represents the typical slope angle of keels.

The sheltering coefficient in Eq. (3) can reach down to -0.44, while in the other two functions, the minimum values were 0.30 and 0.08 when L/H = 2. Such small spacings are uncommon in a real sea ice cover, but ridges sometimes form in closely packed clusters. Valenti et al. (2021) proposed from observations that L follows the lognormal distribution presented by Wadhams and Davy (1986), with the third quartile values Q3 = 292 m and 277 m in the Beaufort and Chukchi Seas, respectively, and the average keel depth is approximately 5-8.5 m. As a result, L/H was mostly in the range of less than 60, accompanied by Γ from -0.14 to 0.93 for α =30° (Eq. 3). Thus, the form drag from ice ridges was significantly weakened due to the sheltering.

498 This effect will be strengthened as the frequency of ice ridges increases during the
499 winter (Steele et al., 1989). Besides, the occurrence of ridge keels tends to be
500 consecutive and overlapping in the spatial underice profiles from the moored IPS and
501 ADCP data of Valenti et al. (2021), resulting in the sheltering of the wake being
502 superimposed and enhanced.

503 The inclination angle of obstacles has been validated in hydrodynamics and sea
504 ice dynamics as a key parameter of the drag force of two square pillars (Du et al.,
505 2019; Yen et al., 2008) and ridge keels (Zu et al., 2021). In particular, the geometry of
506 ridged ice varies greatly for the depth and cross-sectional shape, e.g., a maximum
507 depth of 27 m and a maximum slope angle of 87.5° were observed by Kharitonov &
508 Borodkin (2020). The differences in α depend on many factors, such as wind speed
509 and current direction, which drive sea ice deformation. Observations show keel slopes
510 in the Barents Sea of 8°-29° and in the Shokalsky Strait of 11.2°-87.5° (Sand et al.,
511 2015; Kharitonov & Borodkin, 2020). Neglecting the changes in the slope angle, i.e.,
512 with the fixed angle of 30° in Eq. (3), the form drag on ice ridges in the Barents Sea
513 will be underestimated by 17.7% within L/H = 10-40, while it may be overestimated
514 by as much as 43.5% in the Shokalsky Strait.

515 **5.2 Views on sea ice dynamics**

516 The most significant advance between the new sheltering function Γ and the
517 previous versions Γ_1 and Γ_2 is the includes of the keel angle, inevitably inducing a
518 change in C_{io} in Eq. (2), which further changes the contribution of oceanic drag force
519 τ_{io} in the sea ice momentum equation. In the free-drifting conditions, sea ice motion
520 depends mainly on the wind and current drag forces, providing a good scenario to
521 check the impact of the new sheltering function. Fig 12. shows the variation of C_{io} (a-
522 c), wind factor (the ratio of sea ice drift velocity to wind velocity) $|u_i|/|u_a|$ (d-f) and
523 the deflection angle θ (g-i) calculated using three different sheltering functions (a, d,
524 g: Γ_1; b, e, h : Γ_2 ; c, f, i: Γ in Eq.(3)) with keel geometric parameters H/L and α when
525 A = 0.8. The drag coefficients are calculated using Eq. (2) with reference to the
526 parametrisation scheme of Lu et al. (2011), and the calculation of the wind factor and
527 deflection angle follows the momentum equation of free-drifting sea ice by
528 Leppäranta (2011), with the formulas and parameter values shown in Text S2.
529 Combining data from Valenti et al. (2021) on the distribution of H and L, and
530 observations of H/L from Berner et al. (2021), it can be found that most cases fell
531 within $H/L \geq 0.01$. However, earlier observations show that is predominantly in the
532 range of 0.001-0.01 (Davis & Wadhams, 1995; Granberg & Leppäranta, 1999). As a
533 result, the range of H/L is set to 0.001 to 0.1, covering most keels.

534 Based on Fig. 12(a-c), C_{io} increases as H/L increase but the impact of α is not
535 obvious when $0.001 \leq H/L \leq 0.01$. Differences between the three schemes are clearly
536 visible when $H/L \geq 0.01$. C_{io} is higher with Γ_1 and lower with Γ_2, and in between with
537 Γ. Γ affects C_{io} by changing the contribution of C_r in Eq.(2a). When $H/L \geq 0.01$, C_{io}
538 using Γ varies nonlinearly with the coupling of H/L and α in Fig. 12c, instead of
539 monotonically decreasing as in Fig. 12a and b. L/H and α actions on the wake
540 structure have been illustrated in the PIV results above. The max C_{io} in Fig. 12c only
541 appeared in the region of $0.05 \leq H/L \leq 0.1$ and α=10°-30°.

542 $|u_i|/|u_a|$ is a key indicator of wind stress transfer, determining sea ice drift. Based
543 on the general solution of the free drift equation, $|u_i|/|u_a|$ is a function of Nansen
544 number (Na) and Rossby number (R) where $N\text{a} \propto (C_{ai}/C_{io})^{0.5}$ and $R \propto (C_{ai}C_{io})^{-0.5}$. For
545 $|R|<0.2$, $|u_i|/|u_a| \approx N\text{a} \propto (C_{ai}/C_{io})^{0.5}$ (Leppäranta. 2011). So, $|u_i|/|u_a|$ is in positive
546 correlation with Γ^{-1}. $|u_i|/|u_a|$ are mostly in 0.012-0.024, consistent with the
547 observation of Cole et al. (2017) in the Canada Basin. When $H/L \geq 0.01$, $|u_i|/|u_a|$ also
548 varies nonlinearly due to the sheltering effect. Interestingly, in the range of $0.06 \leq H/L$
549 ≤ 0.1, u_i / u_a reaches its maximum 0.024 when α varied from 10 to 90°, implying the
550 amplification of stress transfer from the atmosphere.

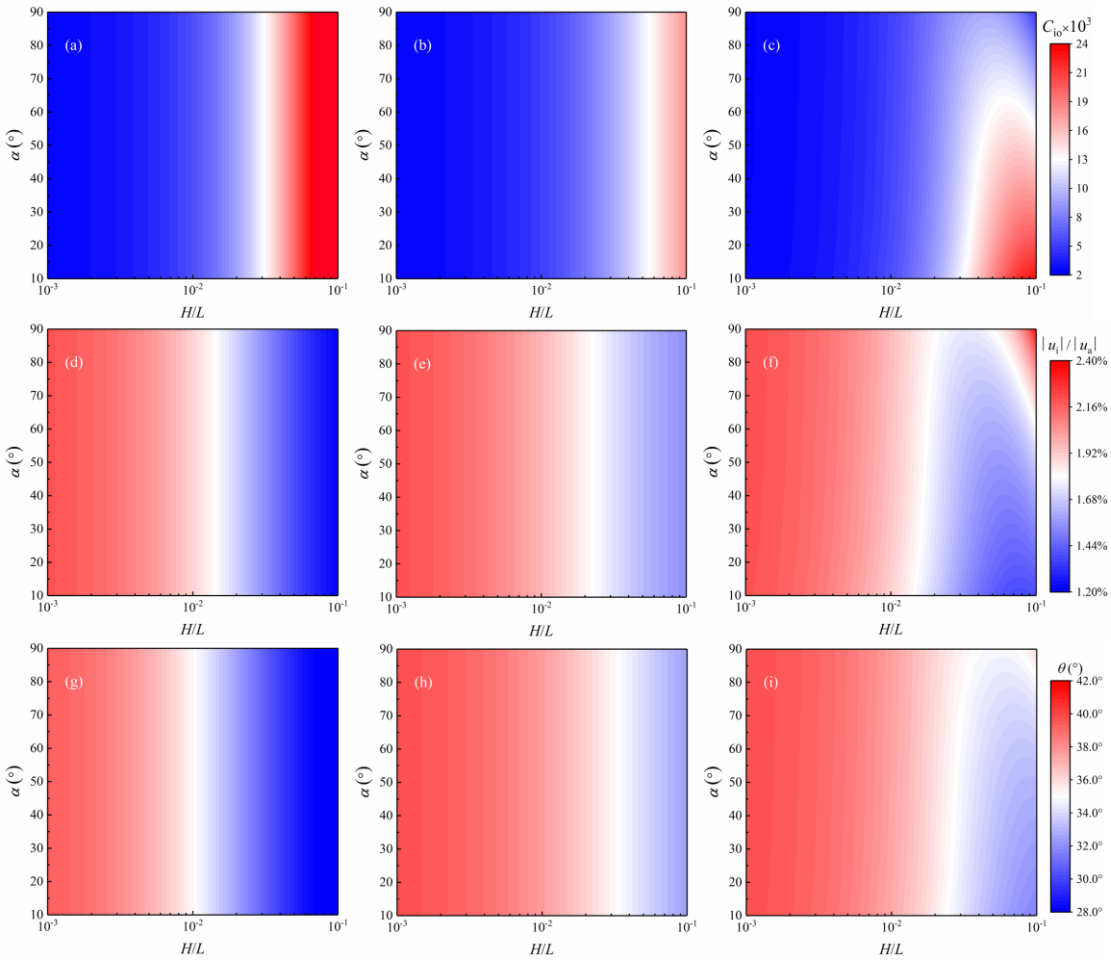

Fig.12 Variation of C_{io}, $|u_i|/|u_a|$ and θ with keel geometric parameters H/L and α when $A = 0.8$: (a, d, g) sheltering function is Γ_1; (b, e, h) Γ_2; (c, f, i) Γ. The drag coefficients are calculated with reference to the parameterization of Lu et al. (2011) and the calculation of $|u_i|/|u_a|$ and θ follows the momentum equation of free-drifting sea ice by Leppäranta (2011), with the formulas and parameter values shown in Text S2.

In the case of $|u_i|/|u_a| \rightarrow Na$, θ can be simplified to a function of R when the surface wind angle and oceanic Ekman angle are given (Leppäranta. 2011). Therefore,

560 θ is a function of $(C_{ai}C_{io})^{-0.5}$, then θ is positively correlated with Γ^{-1}. The variation
561 pattern of θ is independent of the chosen values of wind angle and oceanic Ekman
562 angle for $|R|<0.2$, as shown in Text S2. θ presented in Fig13. i is higher than that in
563 Fig12. g while lower than Fig12. h. With the increasing of H/L from 0.01 to 0.1, θ
564 decreases about 36% when α =30°. With the increasing of α from 10 to 90° when
565 H/L=0.05, θ increases about 24%.

566 **5.3 Laboratory experiments vs. polar oceans - limitations and uncertainties**

567 This paper has been devoted to laboratory experiments on the sheltering effect
568 between ice ridges and a new sheltering function has been proposed. The
569 experimental results provide solid references for parametrisation in sea ice dynamics,
570 but differences in the boundary conditions between the water tank and the Arctic
571 Ocean must be clarified because they partly limit the direct application to polar oceans.
572 Firstly, the upper boundary in the tank was a free surface, while the polar ocean
573 surface is covered with ice. This mainly affects whether the incoming reference
574 velocity is chosen to be a logarithmically-law distributed flow velocity in the inner
575 boundary layer Lüpkes et al., 2012) or the far-field velocity independent of the
576 thickness of the boundary layer (Shaw et al., 2008; Österlund et al., 2000). The inner

577 logarithmic layer is approximately 2 m deep in winter (Kharitonov & Borodkin,
578 2020) and less in summer (Cole et al., 2017; Gallaher et al., 2016), as estimated by
579 an empirical formula related to the Ekman depth (Shaw et al., 2008). Therefore, the
580 logarithmic layer is of concern primarily for small ice ridges in winter.

581 The conversion factors of the two reference velocities for the single keel form
582 drag were derived by Zu et al. (2021) as 1.1-1.3, decreasing with increasing ridge
583 height. However, we are concerned with the effect of the reference velocity on
584 sheltering characterised by F_1/F_2. Section 4.2 showed that the wake generated by a
585 fixed shape keel is independent of u in the turbulent conditions, consistent with the
586 attenuation after passing through the shelterbelt for different wind speeds (Ozawa et
587 al., 2007) and the review of sheltering behind sand fences (Li & Sherman, 2015).
588 Therefore, it is reasonable to assume that the errors introduced by differences in the
589 upper boundary are small and do not significantly impact the form or accuracy of the
590 sheltering function.

591 Secondly, compared to the natural conditions in the Arctic Ocean where $D \gg H$,
592 the shallow water in the experimental tank has led to increased sheltering. To better
593 understand this, we performed variable depth experiments with D varying from 0.30–
594 0.50 when α= 45°, H = 0.12m. The resulting Γ vs. L/H is given in Fig. 13. The dark

595 red curve represents the fit for D = 0.30 m (R^2 = 0.99), while the light red curve
596 represents the fit for D = 0.50 m (R^2 = 0.98). The shallow depth may restrict the
597 ability of wakes to expand vertically, inhibiting the spread of eddies along the depth
598 direction and resulting in accelerated wake recovery (Ouro & Nishino, 2021; Singha
599 et al., 2009; Akilli, & Rockwell, 2002). As a result of this feature, Γ gradually
600 increased with decreasing D. D/H was not inserted in the form of the sheltering
601 function but rather illustrated by the determination of its coefficients. No attempt has
602 been made here to fit depth D into the sheltering function for this stage, because Γ is
603 expected to be depth-independent beyond the critical depth (Zu et al., 2021).
604 However, this does not deny the above evaluations of sea ice dynamic parameters in
605 section 5.2. Because Fig. 12(a-c) was recalculated by using approximately 50% lower
606 coefficients of the exponential function in Eq. (3), but the results revealed that the
607 variation trend changed little and the maximum value of C_{io} increased only below
608 15%. The given portion 50% is roughly determined through linearly extending the
609 form of $\Gamma_{D=0.3}$ and $\Gamma_{D=0.5}$ in Fig.13 to the critical depth in Zu et al. (2021).

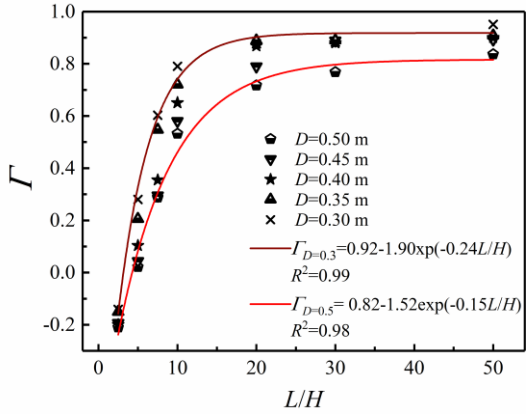

Fig. 13 The sheltering coefficient $\Gamma = \Gamma(L/H)$ when the tank depth D is increased from 0.30 m to 0.50 m at α = 45° and H=0.12 m (D/H=2.5-4.17). The dark red/light red curve represents the fit of Γ for D = 0.30 m/D = 0.50 m; R^2 = 0.99 and 0.98. The fits for the other D are similar, and not shown here.

Thirdly, the sheltering strength of the wake was overestimated in the far-wake region (L/H > 30). Asymptotically, the sheltering function approached a limit less than 1, within 0.82–0.97 in Fig. 11. This was somewhat different from our intuition and was caused by the nature of laboratory experiments where the system is forced by the inflow boundary condition. The flow section in the tank was 11 m long inevitably experienced a loss of flow velocity and the floating free surface which may result in Γ < 1. Since the momentum was fed into the system from the boundary, passing a keel resulted in a loss of momentum due to the form drag. Consequently, the drag force

624 was lower than expected at keel-2, with Γ<1. In nature, momentum is fed into the
625 system by distributed forcing over the whole ice cover, and a corresponding
626 momentum loss does not occur. Thus, when the ridge spacing tends to infinity, the
627 downstream keel drag force is not affected by upstream sheltering, corresponding to
628 Γ=1.

629 **5 Conclusion**

630 Laboratory experiments were carried out to investigate the form drag of adjacent
631 sea ice ridges and the sheltering effect of varying keel depth H, dimensionless spacing
632 L/H, keel slope angle α, and flow velocity u. The conclusions are drawn as below.

633 The drag force F_1 on the upstream keel exhibited stability as L/H increased and
634 was close to the case of an individual keel; just within L/H <10, F_1 increased by 5%
635 due to the presence of downstream keel. The drag force F_2 on the downstream keel
636 became larger with increasing L/H and gradually approached an asymptote. At $L/H \leq$
637 10, F_2 was opposite to the flow direction, as the downstream keel was located within
638 the recirculation zone created by the upstream one. F_2 was proportional to the square
639 of u, consistent with the classical drag force formula.

640 The sheltering coefficient $\Gamma = F_2/F_1$ characterises the sheltering strength. Γ is

641 related to L/H and α but is independent of u. A new formula was proposed by fitting
642 the experimental results: $\Gamma = [1\text{-}1.56\exp(sL/H)]\times 1.20\alpha^{-0.08}$, $s = 0.001\alpha\text{-}0.15$; s was
643 changed from a constant to a linear function of α. Overall, the function can be treated
644 as the product of an exponential function and a power function. On the one hand,
645 there is an exponential relationship between Γ and L/H. Γ increased as the L/H
646 increases and underwent the transition from negative to positive at L/H = 5. The time-
647 averaged streamlines, turbulent kinetic energies and Reynolds stresses for L/H = 5 and
648 L/H = 10, corresponding to the single body regime and the reattached flow regime,
649 were calculated using the PIV results to validate the effect of L/H variations on wake
650 turbulence characteristics. On the other hand, there is a power relationship between Γ
651 and α which is characterised a decreasing trend as α increases. By comparing the flow
652 flied results for α = 20°, 45° and 60°, the wake expanded longitudinally as the angle
653 increased, accompanied by larger recirculation zone, stronger TKE, and greater
654 Reynolds stress. However, the influence of α on Γ was also coupled with L/H. α was
655 mostly impactful in the near-wake region.

656 A sea ice free-drift dynamics case was calculated using three different sheltering
657 function. The differences in results of C_{io}, wind factor $|u_i|/|u_a|$ and the deflection angle
658 θ are more pronounced at $H/L \geq 0.01$, corresponding to more dense ridged ice

659 nowadays in observations than before (Berner et al. 2021; Davis & Wadhams, 1995).
660 The values calculated using the new sheltering function are larger than the power
661 function, smaller than the exponential function. The coupling of H/L and α leads to a
662 non-linear variation of C_{io}, $|u_i|/|u_a|$ and θ at $H/L \geq 0.01$, however, the remaining two
663 functions could not to capture this feature. In the range of $0.05 \leq H/L \leq 0.1$, the
664 sheltering strength is enhanced and $|u_i|/|u_a|$ increases from 0.012 to 0.024 when α
665 increased from 10 to 90°. It is contrast to a constant wind factor for different ridge
666 slope as using previous sheltering functions.

667 As a solid step towards the final objective of parameterization, the new function
668 has a clear physical meaning that incorporates both the impact of the dimensionless
669 spacing and slope angle on the sheltering, which is an improvement of the previous
670 results by Steele et al. (1989). The outcome has clarified the major parameters
671 affecting sheltering as well as the turbulent structure and characteristics of the flow
672 field around double keels. Because of the limitations from water tank experiments,
673 Eq. (3) cannot be further optimised and then directly applied to the polar ocean.
674 However, it can be straightforwardly improved and extended to depth-independent
675 situations using numerical simulations in the next step. Possible directions of future
676 research include, but are not limited to, (i) considering the probability distribution

function of geometric parameters and spacings of ice ridges, (ii) considering the porosity of ice ridges, and (iii) probing the mechanisms of variation in shelter effects in a stratified two-layer flow. It is anticipated that a universal relationship can be obtained that is applicable in sea ice dynamics modelling.

Acknowledgements

This research was supported by the National Key R&D Program of China (2023YFC2809102), the National Natural Science Foundation of China (Grant Nos. 42320104004, 52192692, and 42276242), and the Academy of Finland (Grant No. 333889).

Data Availability Statement

The laboratory experiment data include drag force measurements and PIV flow field measurements shown in this manuscript can be accessed via the website (https://doi.org/10.5281/zenodo.10065506)

References

Albedyll, L. V., Haas, C., & Dierking, W. (2021). Linking sea ice deformation to ice

693 thickness redistribution using high-resolution satellite and airborne observations. *The*
694 *Cryosphere*. 15, 2167–2186. https://doi.org/10.5194/tc-15-2167-2021
695 Armitage, T. W. K., Manucharyan, G. E., Petty, A. A., Kwok, R., & Thompson, A. F.
696 (2020). Enhanced eddy activity in the Beaufort Gyre in response to sea ice loss.
697 *Nature Communications*, 11(1), 761. https://doi.org/10.1038/s41467-020-14449-z
698 Arya, S. P. S. (1975). A drag partition theory for determining the large-scale
699 roughness parameter and wind stress on the Arctic pack ice. *Journal of Geophysical*
700 *Research*, 80(24), 3447-3454. https://doi.org/10.1029/JC080i024p03447
701 Akilli, H., & Rockwell, D. (2002). Vortex formation from a cylinder in shallow water:
702 Flow Structure and Topology. *Physics of Fluids*, 14(9), 2957-2967.
703 https://doi.org/10.1063/1.1483307
704 Boutin, G., Ardhuin, F., Dumont, D., Sévigny, C., Girard-Ardhuin, F., & Accensi, M.
705 (2019). Floe size effect on wave-ice interactions: possible effects, implementation in
706 wave model, and evaluation. *Journal of Geophysical Research*: *Oceans*, 123(7), 4779-
707 4805. https://doi.org/10.1029/2017JC013622
708 Brenner, S. D., Rainville, L., Thomson, J., Cole, S. T., & Lee, C. M. (2021).
709 Comparing observations and parameterisations of ice-ocean drag through an annual
710 cycle across the Beaufort Sea. *Journal of Geophysical Research: Oceans*, 126(4),

711 e2020JC016977. https://doi. org/10.1029/2020JC016977

712 Castellani, G., Lüpkes, C., Hendricks, S., & Gerdes, R. (2014). Variability of Arctic
713 sea-ice topography and its impact on the atmospheric surface drag. J*ournal of*
714 *Geophysical Research: Oceans*, 119(10), 6743–6762.
715 https://doi.org/10.1002/2013JC009712

716 Castellani, G., Losch, M., Ungermann, M., & Gerdes, R. (2018). Sea-ice drag as a
717 function of deformation and ice cover: Effects on simulated sea ice and ocean
718 circulation in the Arctic. *Ocean Modelling*, 128, 48–66.
719 https://doi.org/10.1016/j.ocemod.2018.06.002

720 Davis, N. R., & Wadhams, P. (1995). A statistical analysis of Arctic pressure ridge
721 morphology. *Journal of Geophysical Research*, 100(C6), 10915-10925.
722 https://doi.org/10.1029/95JC00007

723 Du, X., Xu, H., Ma, W., Dai, C., & Liu, Q. (2019). Experimental study on
724 aerodynamic characteristics of two square cylinders at various incidence angles.
725 *Journal of Wind Engineering & Industrial.* 191, 154-169.
726 https://doi.org/10.1016/j.jweia.2019.05.019

727 Gallaher, S. G., Stanton, T. P., Shaw, W. J., Cole, S. T., Toole, J. M., Wilkinson, J. P.,
728 Maksym, T., & Hwang, B. (2016). Evolution of a Canada Basin ice-ocean boundary

729 layer and mixed layer across a developing thermodynamically forced marginal ice
730 zone, *Journal of Geophysical Research: Oceans*, 121, 6223–6250,
731 https://doi.org/10.1002/2016JC011778
732 Garbrecht, T., Lüpkes, C., Augstein, E., & Wamser, C. (1999). Influence of a sea ice
733 ridge on low-level airflow. *Journal of Geophysical Research*, 104(D20), 24499-24507.
734 https://doi.org/10.1029/1999JD9004810.1029/1999jd900488
735 Garbrecht, T., Lüpkes, C., Hartmann, J., & Wolff, M. (2002). Atmospheric drag
736 coefficients over sea ice-validation of a parameterisation concept. *Tellus A: Dynamic*
737 *Meteorology and Oceanography*, 54(2), 205–219.
738 https://doi.org/10.3402/tellusa.v54i2.12129
739 Hanssen-Bauer, I., & Gjessing, Y. T. (1988). Observations and model calculations of
740 aerodynamic drag on sea ice in the Fram Strait. *Tellus A*, 40, 151-161.
741 https://doi.org/10.1111/j.1600-0870.1988.tb00413.x
742 Herman, A. (2011). Molecular-dynamics simulation of clustering processes in sea-ice
743 floes. *Physical Review*, E, 84, 056104. https://doi.org/10.1103/PhysRevE.84.056104
744 Itkin, P., Spreen, G., Cheng, B., Doble, M., Girard-Ardhuin, F., Haapala, J., Hughes,
745 N., Kaleschke, L., Nicolaus, M., & Wilkinson, J. (2017), Thin ice and storms: Sea ice
746 deformation from buoy arrays deployed during N-ICE2015, *Journal of Geophysical*

Research: Oceans, 122, 4661–4674. https://doi.org/10.1002/2016JC01240

Jian, H., Wang, Z., Wang, Z., Sun, S., Sun, C. & Guo, C. (2020). Numerical Simulation on Vortex Shedding from a Hydrofoil in Steady Flow. *Journal of Marine Science and Engineering*, 8(3), 195. https://doi.org/10.3390/jmse8030195

Jin, Z., Dong, Q., & Yang, Z. (2014). A stereoscopic PIV study of the effect of rime ice on the vortex structures in the wake of a wind turbine. *Journal of Wind Engineering & Industrial Aerodynamics*, 134:139-148. https://doi.org/10.1016/j.jweia.2014.09.001

Kaleschke, L., Nicolaus, M., & Wilkinson, J. (2017), Thin ice and storms: Sea ice deformation from buoy arrays deployed during N-ICE2015, *Journal of Geophysical Research: Oceans*, 122, 4661–4674, https://doi.org/10.1002/2016JC01240

Kharitonov, V. V., & Borodkin, V. A. (2020). On the results of studying ice ridges in the Shokal'skogo Strait, part I: Morphology and physical parameters in-situ. *Cold Regions Science and Technology*, 174, 103041. 41. https://doi.org/10.1016/j.coldregions.2020.103041

Kim, M., Kim, D., Yoon, S., & Lee, D. (2008). Measurements of the flow fields around two square cylinders in a tandem arrangement. *Journal of Mechanical Science & Technology*, 22(2), 397. https://doi.org 10.1007/s12206-007-1041-6

765 Kumar, D., & Sen, S. (2021). Flow-induced vibrations of a pair of in-line square
766 cylinders. *Physics of Fluids.* 33, 043602. https://doi.org/10.1063/5.0038714.
767 Kwok, R. (2018). Arctic sea ice thickness, volume, and multiyear ice coverage:
768 Losses and coupled variability (1958-2018). *Environmental Research Letters*, 13(10).
769 105005. https://doi.org/10.1088/1748-9326/aae3ec
770 Kurtulmuş, N. (2022). Flow past two tandem square cylinders placed in parallel walls.
771 *Ocean Engineering*. 262, ISSN 0029-8018,
772 https://doi.org/10.1016/j.oceaneng.2022.112352.
773 Lemieux, J.-F., Tremblay, L. B., Dupont, F., Plante, M., Smith, G. C., & Dumont, D.
774 (2015). A basal stress parameterisation for modeling landfast ice, *Journal of*
775 *Geophysical Research: Oceans*, 120, 3157–3173, https://doi.org/10.1002/
776 2014JC010678
777 Leppäranta, M. (2011). The drift of sea ice, 2nd ed. Berlin: Springer.
778 Leppäranta, M., & Granberg, B. H. (1999). Observations of sea ice ridging in the
779 Weddell Sea. *Journal of Geophysical Research.* 104(c11), 25735-
780 25745.https://doi.org/10.1029/1999JC900160
781 Leppäranta, M., Lensu, M., Kosloff, P., & Veitch, B. (1995). The life story of a first-
782 year sea ice ridge. *Cold Regions Science and Technology* 23: 279–290.

https://doi.org/10.1016/0165-232X(94)00019-T

Leppäranta, M. & Omstedt, A. (1990). Dynamic coupling of sea ice and water for an ice field with free boundaries. *Tellus* **42**A: 482–495. https://doi.org/10.1034/j.1600-0870.1990.t01-2-00007.x

Li, B., & Sherman, D. J. (2015). Aerodynamics and morphodynamics of sand fences: a review. *Aeolian Research*, 17, 33-48. https://doi.org/10.1016/j.aeolia.2014.11.005

Li, Z., Abrahamsenprsic, M., Ong, M., & Khoo, B. (2018). Large eddy simulations of flow around two circular cylinders in tandem in the vicinity of a plane wall at small gap ratios. *Journal of fluids and structures.*76, 251-271. https://doi.org/10.1016/j.jfluidstructs.2017.10.006

Liu, C., & Chen, J. (2002). Observations of hysteresis in flow around two square cylinders in a tandem arrangement. *Journal of Wind Engineering and Industrial Aerodynamics*, 90(9), 1019-1050. https://doi.org/10.1016/S0167-6105(02)00234-9

Lin, J., Yang, Y., & Rockwell, D. (2002). Flow past two cylinders in tandem: instantaneous and averaged flow structure. *Journal of Fluids and Structures*, 16(8), 1059-1071. https://doi.org/10.1006/jfls.2002.0469

Lopez, S. C., Lüpkes, C., & Schlünzen, K. H. (2005), The effect of different k-ε closures on the results of a micro-scale model for the flow in the obstacle layer,

Meteorol. Z., 14(6), 839–848. https://doi.org/10.1127/0941-2948/2005/0084

Luo, S., Li, L., & Shah, D. (1999). Aerodynamic stability of the downstream of two tandem square-section cylinders. *Journal of Wind Engineering and Industrial Aerodynamics*, 79(1), 79-103. https://doi.org/10.1016/S0167-6105(98)00111-1

Lu, P., Li, Z., Cheng, B., & Leppäranta, M. (2011). A parameterisation of the ice-ocean drag coefficient. *Journal of Geophysical Research*, 116, C07019. https://doi.org/10.1029/2010JC006878

Lu, P., Li, Z., & Han, H. (2016). Introduction of parameterized sea ice drag coefficients into ice free-drift modeling. Acta Oceanologica Sinica, 35(1): 53–59, https://doi.org/ 10.1007/s13131-016-0796-y

Lüpkes, C., Gryanik, V. M., Hartmann, J., & Andreas, E. L. (2012). A parametrization, based on sea ice morphology, of the neutral atmospheric drag coefficients for weather prediction and climate models. *Journal of Geophysical Research*, 117(D13). https://doi.org/10.1029/2010JC006878

Mai, S., Wamser, C., & Kottmeier, C. (1996). Geometric and aerodynamic roughness of sea ice. *Boundary-Layer Meteorology*, 77, 233-248. https://doi.org/10.1007/BF00123526

Martinson, D. G., & Wamser, C. (1990). Ice drift and momentum exchange in winter

819 Antarctic pack ice. *Journal of Geophysical Research Atmospheres*, 95(C2), 1741-1755.
820 https://doi.org/10.1029/JC095iC02p01741
821 Mårtensson, S., Meier, H. E. M., Pemberton, P., & Haapala, J. (2012). Ridged sea ice
822 characteristics in the Arctic from a coupled multicategory sea ice model. *Journal of*
823 *Geophysical Research*, 117(C8). https://doi.org/10.1029/2010JC006936
824 Martin, T., Tsamados, M., Schroeder, D., & Feltham, D. L. (2016). The impact of
825 variable sea ice roughness on changes in Arctic Ocean surface stress: A model study.
826 *Journal of Geophysical Research: Oceans*, 121(3), 1931-1952. 2.
827 https://doi.org/10.1002/2015JC011186
828 Melling, H., & Riedel, D. (1995). The underside topography of sea ice over the
829 continental shelf of the Beaufort Sea in the winter of 1990. *Journal of Geophysical*
830 *Research: Oceans*, 100(C7):13641-13653. https://doi.org/10.1029/95JC00309
831 Metzger, A. T., Mahoney, A. R., & Roberts, A. F. (2021). The average shape of sea ice
832 ridge keels. *Geophysical Research Letters*, 48, e2021GL095100.
833 https://doi.org/10.1029/2021GL095100
834 McPhee, M. G. (2002). Turbulent stress at the ice/ocean interface and bottom surface
835 hydraulic roughness during the SHEBA drift. *Journal of Geophysical Research*,
836 107(C10), 8037. https://doi.org/10.1029/2000JC000633

837 McPhee, M. G. (2008). Air-ice-ocean interaction: Turbulent ocean boundary layer
838 exchange processes. *Springer-Verlag*. https://doi. org/10.1007/978-0-387-78335-2
839 Mai, S., Wamser, C., & Kottmeier, C. (1996). Geometric and aerodynamic roughness
840 of sea ice. *Boundary-Layer Meteorology*, 77, 233-248.
841 https://doi.org/10.1007/BF00123526
842 Morison, J., & Dan, G. (2012). A brief study of the force balance between a small
843 iceberg, the ocean, sea ice, and atmosphere in the Weddell Sea. *Cold Regions Science*
844 *& Technology*, 76-77(none):69-76. https://doi.org/10.1016/j.coldregions.2011.10.014
845 Mortikov, E. V. (2016). Numerical simulation of the motion of an ice keel in a
846 stratified flow. *Izvestiya, Atmospheric and Oceanic Physics*, 52(1), 120-128.
847 https://doi.org/10.1134/S0001433816010072
848 Nägeli, W. (1964). Further investigation of the wind conditions in areas with
849 shelterbelts (in German). *Mitt. Schweiz. Anstalt Forstl*, 24, 659-737.
850 Notz, D., & Stroeve, J. (2018). The trajectory towards a seasonally ice-free Arctic
851 Ocean. *Current Climate Change Reports*, 4(4), 407–416.
852 https://doi.org/10.1007/s40641-018-0113-2
853 Österlund, J. M., Johansson, A. V., Nagib, H. M., & Hites, M. H. (2000). A note on the
854 overlap region in turbulent boundary layers. *Physics of Fluids*, 12(1), 1-4.

855 https://doi.org/10.1063/1.870250.

856 Ouro, P., Wilson, C. A. E., Evans, P., & Angeloudis, A. (2017). Large-eddy simulation
857 of shallow turbulent wakes behind a conical island. *Physics of Fluids*, 29, 126601.
858 https://doi.org/10.1063/1.5004028

859 Ouro, P., & Nishino, T. (2021). Performance and wake characteristics of tidal turbines
860 in an infinitely large array. *Journal of Fluid Mechanics.* 925, A30,
861 https://doi.org/10.1017/jfm.2021.692.

862 Ozawa, H., Sakamoto, T., & Hagino, H. (2007). Influence of thinning on the shelter
863 effect of windbreaks as clarified by a wind tunnel experiment. *Journal of Forest*
864 *Research*, 12(3), 222-229. https://doi.org/10.1007/s10310-007-0006-z

865 Prinsenberg, S., & Peterson, I. K. (2002). Variations in air-ice coefficient due to ice
866 surface roughness. *International Journal of Offshore and Polar Engineering*, 12(2),
867 121-125. https://doi.org/10.1109/TITS.2002.801421

868 Pite, H. D., Topham, D. R., & van Hardenberg, B. J. (1995). Laboratory
869 measurements of the drag force on a family of two-dimensional ice keel models in a
870 two-layer flow. *Journal of Physical Oceanography*, 25, 3008-3031.
871 https://doi.org/10.1175/1520-0485(1995)0252.0.co;2

872 Pinarbasi, A., Pinar, E., Akilli, H., & Ince, E. (2015). Shallow water experiments of

flow past two identical square cylinders in tandem. *European Journal of Mechanics / B Fluids*, 49, 100-107. https://doi.org/10.1016/j.euromechflu.2014.08.009

Rampal, P., Weiss, J., & Marsan, D. (2009). Positive trend in the mean speed and deformation rate of arctic sea ice, 1979–2007. *Journal of Geophysical Research: Oceans*. 13, https://doi.org/10.1029/2008JC005066

Reza, M., Arcondoulis, E. J. G., Qian, L., & Yu, L. (2023). Experimental near-field analysis for flow induced noise of a structured porous-coated cylinder. *Journal of Sound and Vibration*, 551. https://doi.org/10.1016/j.jsv.2023.117611

Roach, L. A., Horvat, C., Dean, S. M., & Bitz, C. M. (2018). An emergent sea ice floe size distribution in a global coupled ocean-sea ice model. *Journal of Geophysical Research: Oceans*, 123(6), 4322–4337. https://doi.org/10.1029/2017JC013692

Roberts, A. F., Hunke, E. C., Kamal, S. M., Lipscomb, W. H., Horvat, C., & Maslowski, W. (2019). A variational method for sea ice ridging in Earth system models. *Journal of Advances in Modeling Earth Systems*, 11, 771–805. https://doi.org/10.1029/2018MS001395

Rollin, E. (1983). The influence of wind speed and direction on the reduction of wind speed leeward of a medium porous hedge. *Agricultural Meteorology.* 30, 25–34. https://doi.org/10.1016/0002-1571(83)90038-9

Ryan, P. A. & Münchow, A. (2017). Sea ice draft observations in Nares Strait from 2003 to 2012. *Journal of Geophysical Research: Oceans*, 122, 3057–3080. https://doi.org/10.1002/2016JC011966

Rui, M., & Sangra, P. (2012). Complex geophysical wake flows madeira archipelago case study. *Ocean dynamics*.62(5),683-700, https://doi.org/10.1007/s10236-012-0528-6

Sand, B., Bonath, V., Sudom, D., & Petrich, C. (2015). Three years of measurements of first year ridges in the Barents Sea and Fram Strait. *Paper presented at 23rd International conference on port and ocean engineering under Arctic conditions.* Norway: Trondheim.

Sakamoto, H., Hainu, H., & Obata, Y. (1987). Fluctuating forces acting on two square prisms in a tandem arrangement. *Journal of Wind Engineering and Industrial Aerodynamics*. 26 (1), 85–103, 8. https://doi.org/10.1016/0167-6105(87)90037-7

Shaw, W. J., Stanton, T. P., McPhee, M. G., & Kikuchi, T. (2008). Estimates of surface roughness length in heterogeneous under-ice boundary layers. *Journal of Geophysical Research: Oceans*. 113, C08030, https://doi.org/10.1029/2007JC004550

Shen, G. & Xiang, W. (2002). Similarity analysis of ocean internal waves. *Journal of Tianjin University (Natural Science and Engineering Technology Edition)*.35 (6), 691-

695

Singha, A., Balachandar, R., & Shinneeb, A. M. (2009). PIV-pod investigation of the wake of a sharp-edged flat bluff body immersed in a shallow channel flow. *Journal of Fluids Engineering*, 131(2). https://doi.org/10.1115/1.3054283

Steele, M., Morison, J. H., & Untersteiner, N. (1989). The partition of air-ice-ocean momentum exchange as a function of ice concentration, floe size, and draft. *Journal of Geophysical Research*, 94(C9), 12739–12750. https://doi.org/10.1029/JC094iC09p12739

Stroeve, J., Barrett, A., Serreze, M., & Schweiger, A. (2014). Using records from submarine, aircraft and satellites to evaluate climate model simulations of Arctic sea ice thickness. *The Cryosphere*, 8, 1839–1854. https://doi.org/10.5194/tc-8-1839-2014

Sohankar, A. (2012). A numerical investigation of the flow over a pair of identical square cylinders in a tandem arrangement. *International Journal for Numerical Methods in Fluids.* 70 (10), 1244–1257. https://doi.org/10.1002/fld.2739

Strub-Klein, L., & Sudom, D. (2012). A comprehensive analysis of the morphology of first-year sea ice ridges. *Cold Regions Science and Technology*, 82, 94–109. https://doi.org/10.1016/j.coldregions.2012.05.014

Tennekes, H., Lumley, J. L. (1972). A First Course in Turbulence. Cambridge:

927 MIT Press.

928 Thielen, K. (2021). Sea ice effects on the upper ocean: internal waves, ice-covered
929 gyres and the seasonal ice zone, (Doctoral dissertation). United Kingdom: University
930 of Oxford.

931 Timco, G. W., & Burden, R. P. (1997) An analysis of the shapes of sea ice ridges.
932 *Cold Regions Science and Technology*, 25, 65–77. https://doi.org/10.1016/S0165-
933 232X(96)00017-1

934 Tsamados, M., Feltham, D. L., Schroeder, D., & Flocco, D. (2014). Impact of variable
935 atmospheric and oceanic form drag on simulations of Arctic sea ice. *Journal of*
936 *Physical Oceanography*, 44(5), 1329-1353. https://doi.org/10.1175/JPO-D-13-0215.1

937 Tschudi, M., Meier, W. N., & Stewart, J. S. (2020). An enhancement to sea ice motion
938 and age products at the National Snow and Ice Data Center (NSIDC). *The Cryosphere*,
939 14(5):1519-1536. https://doi.org/10.5194/tc-14-1519-2020

940 Valenti, V., Mahoney, A., & Metzger, A. (2021). A probabilistic description of
941 pressure ridge width, spacing, and keel depth for the Chukchi and Beaufort seas based
942 on IPS and ADCP observations. *Cold regions science and technology*. 182.
943 https://doi.org/10.1016/j.coldregions.2020.103171

944 Vihma, T., Pirazzini, R., Fer, I., Renfrew, I. A., Sedlar, J., & Tjernstr, M. M. (2014).

945 Advances in understanding and parameterisation of small-scale physical processes in
946 the marine arctic climate system: a review. *Atmospheric Chemistry and Physics*, 14,
947 9403–9450, https://doi.org/10.5194/acp-14-9403-2014

948 Wadhams, P., Hughes, N., & Rodrigues, J. (2011). Arctic sea ice thickness
949 characteristics in winter 2004 and 2007 from submarine sonar transects. *Journal of*
950 *Geophysical Research*, 116. https://doi.org/10.1029/2011JC006982

951 Wamser, C., & Martinson, D. G. (1993). Drag coefficients for winter Antarctic pack
952 ice. *Journal of Geophysical Research Atmospheres*, 98(C7):12431-12437.
953 https://doi.org/10.1029/93JC00655

954 Wang, C. H. J., Zhao, D., Schlueter, J., Holzaepfel, F., & Stephan, A. (2017). LES
955 study on the shape effect of ground obstacles on wake vortex dissipation. *Aerospace*
956 *Science & Technology*, 63(Apr.), 245-258. https://doi.org/10.1016/j.ast.2016.12.032

957 Wang, S., Lu, P., Zu, Y., Zhang, L., Wang, Q., & Li, Z. (2022). Experimental Study on
958 the Sheltering Effect between Ice Ridges on Ice-Water Drag Force. *Haiyang*
959 *Xuebao*.44(7),170-176. https://doi.org/10.12284/hyxb2022104

960 Waters, J. K., & Bruno, M. S. (1995). Internal wave generation by ice floes moving in
961 stratified water: Results from a laboratory study. *Journal of Geophysical Research:*
962 *Oceans*, 100(C7): 13635−13639. https://doi.org/10.1029/95JC01220

963 Westerweel, J., Elsinga, G. E., & Adrian, R. J. (2013). Particle image velocimetry for
964 complex and turbulent flows. *Annual Review of Fluid Mechanics*, 45(1), 409.
965 Whale, J., Anderson, C.G., Bareiss, R., & Wagner, S. (2000). An experimental and
966 numerical study of the vortex structure in the wake of a wind turbine. *Journal of Wind*
967 *Engineering and Industrial Aerodynamics*, 84,1-21. https://doi.org/10.1016/S0167-
968 6105(98)00201-3
969 Williamson, C. H. K. (1996). Vortex dynamics in the cylinder wake. *Annual Review of*
970 *Fluid Mechanics*, 28(1), 477-539. Vol. 28:477-539
971 https://doi.org/10.1146/annurev.fl.28.010196.002401
972 Wu Y. (2016). Numerical simulation of the influence of ice ridge on the flow field
973 under ice. (Master's thesis), Dalian University of technology, Dalian, China. China-
974 national-knowledge-internet: http://cdmd.cnki.com.cn/Article/CDMD-10141-
975 1016219988.htm
976 Xue Q., Liang S., Sun Z., Xu Y., & Tian Z. R. (2023). Near-surface characteristics of
977 velocity profile and momentum transport after wave-breaking in deep water. *Ocean*
978 *Engineering*, 276, https://doi.org/10.1016/j.oceaneng.2023.114223
979 Yen, S. C., San, K. C., & Chuang, T. H. (2008). Interactions of tandem square
980 cylinders at low Reynolds numbers. *Experimental Thermal and Fluid Science*. 32,

927–938. https://doi.org/10.1016/j.expthermflusci.2007.07.001

Zhang, J., Schweiger, A., Steele, M., & Stern, H. (2015). Sea ice floe size distribution in the marginal ice zone: Theory and numerical experiments. *Journal of Geophysical Research: Oceans*, 120(5), 3484–3498. https://doi.org/10.1002/2015JC010770

Zu, Y., Lu, P., Leppäranta, M., Cheng, B., & Li, Z. (2021). On the form drag coefficient under ridged ice: laboratory experiments and numerical simulations from ideal scaling to deep water. *Journal of Geophysical Research: Oceans*. 126, e2020JC016976. https:// doi.org/10.1029/2020JC016976.

Figure 1.

(a)

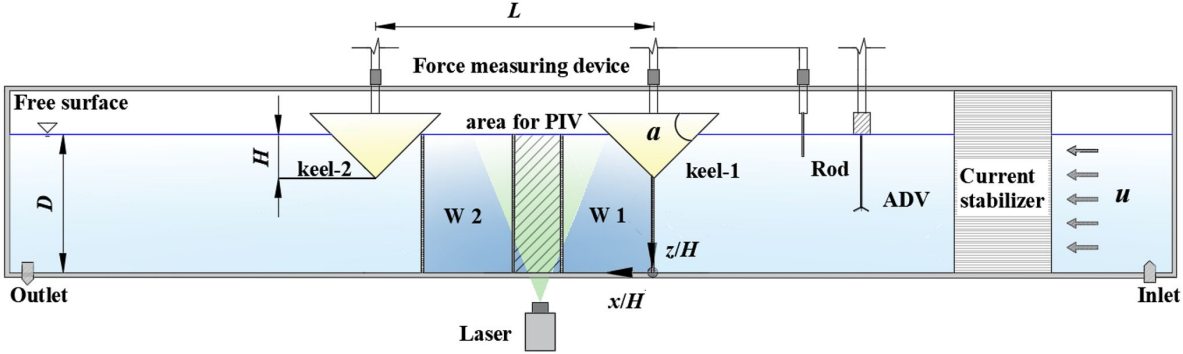
L
Force measuring device
Free surface
area for PIV
a
H
keel-2
keel-1
Rod
ADV
Current stabilizer
u
D
W 2
W 1
z/H
x/H
Outlet
Inlet
Laser

(b)

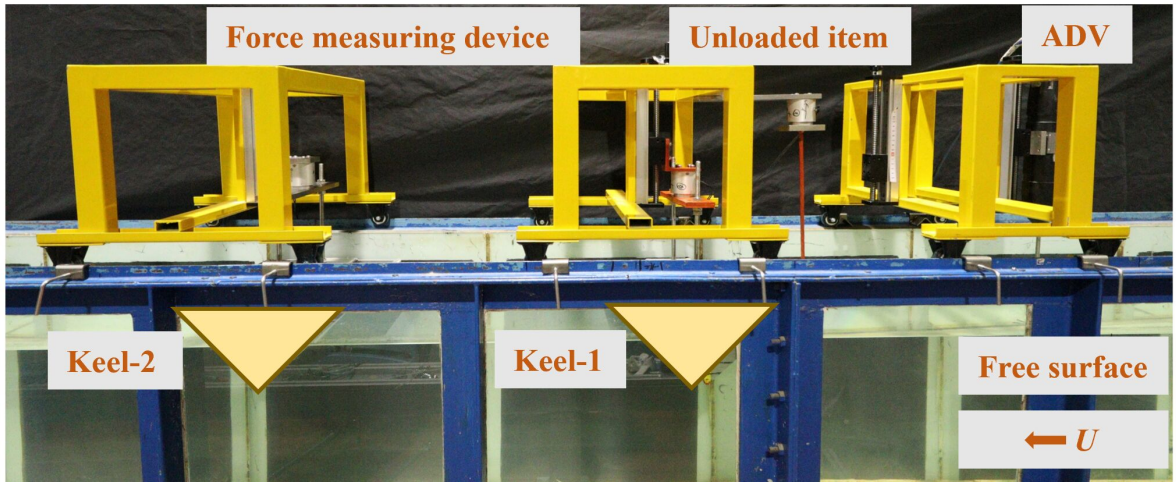
Force measuring device
Unloaded item
ADV
Keel-2
Keel-1
Free surface
U

Figure 2.

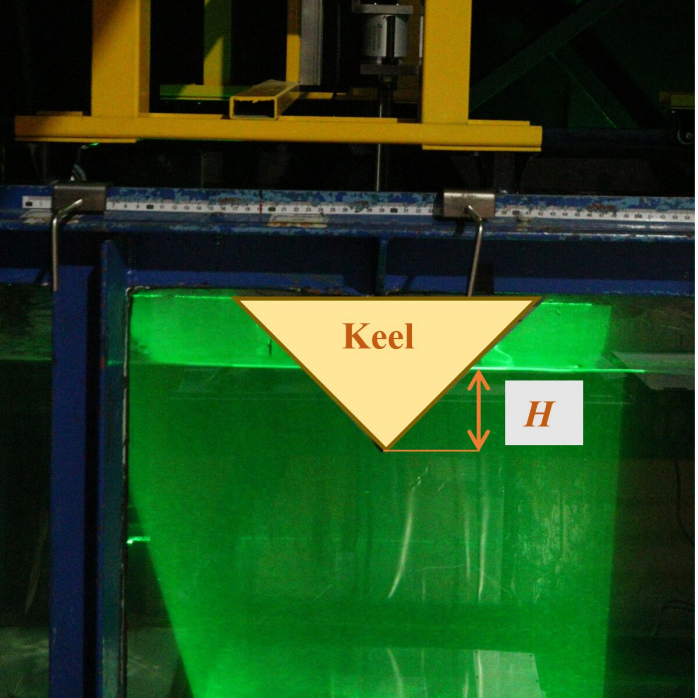
Keel
H


Photron

Figure 3.

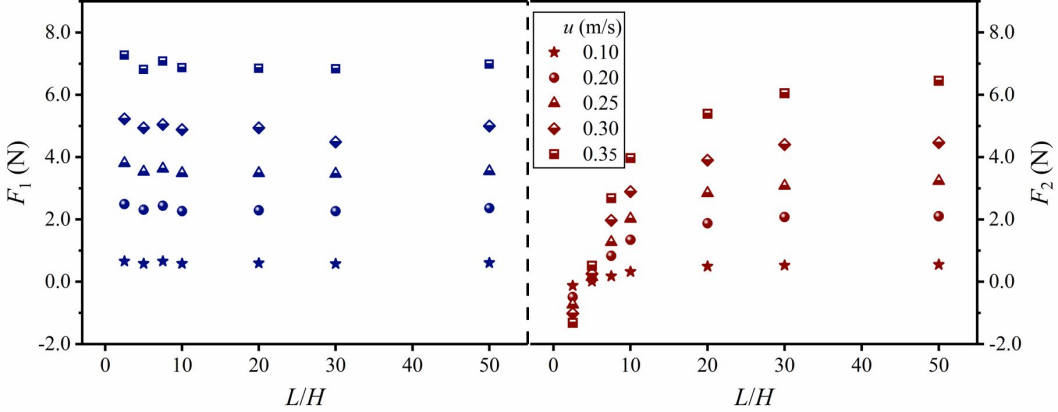
F_1 (N)
F_2 (N)
L/H
L/H
u (m/s)
0.10
0.20
0.25
0.30
0.35
8.0
6.0
4.0
2.0
0.0
-2.0
0
10
20
30
40
50

Figure 4.

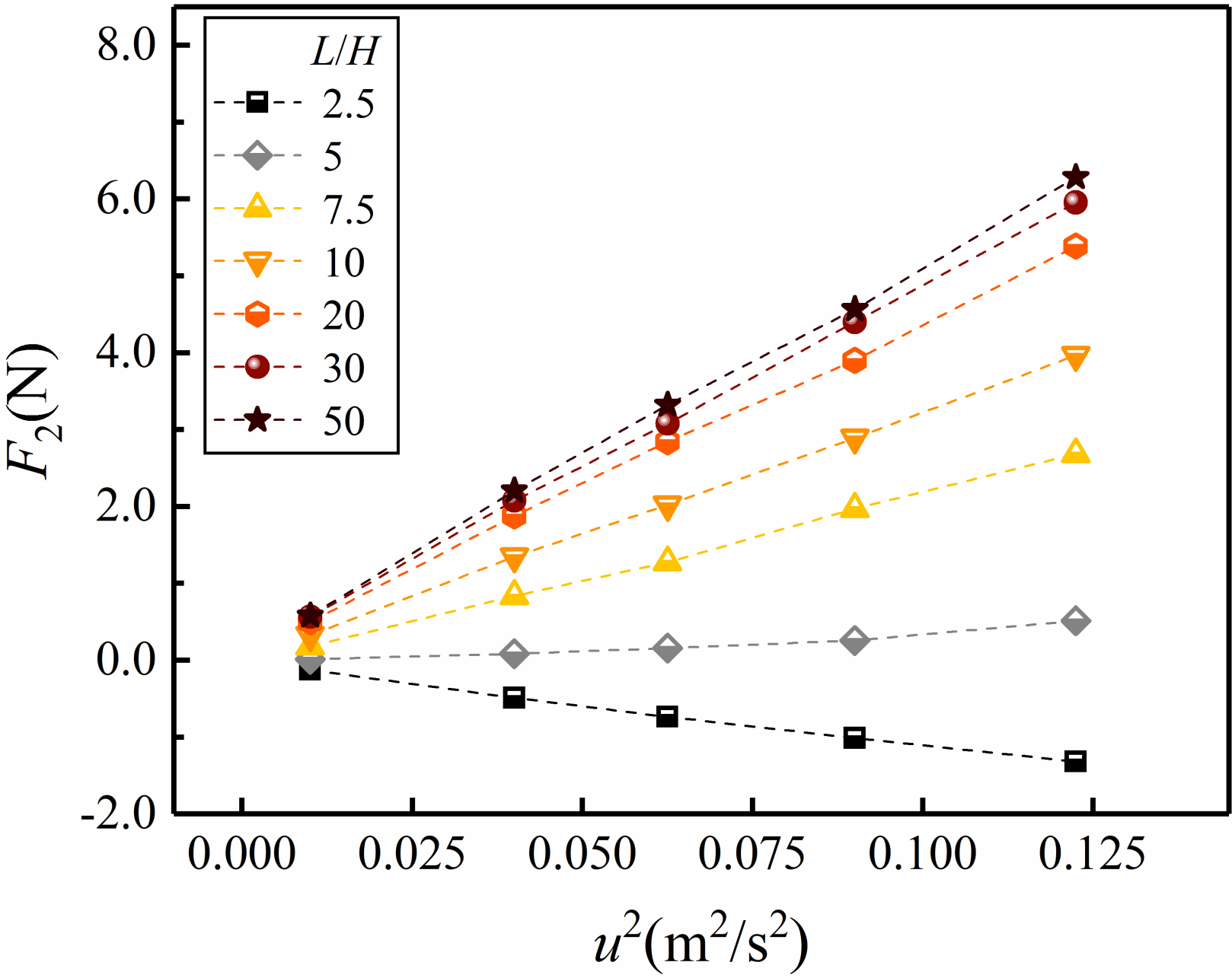
L/H
2.5
5
7.5
10
20
30
50
8.0
6.0
4.0
2.0
0.0
-2.0
F2(N)
0.000
0.025
0.050
0.075
0.100
0.125
u2(m2/s2)

Figure 5.

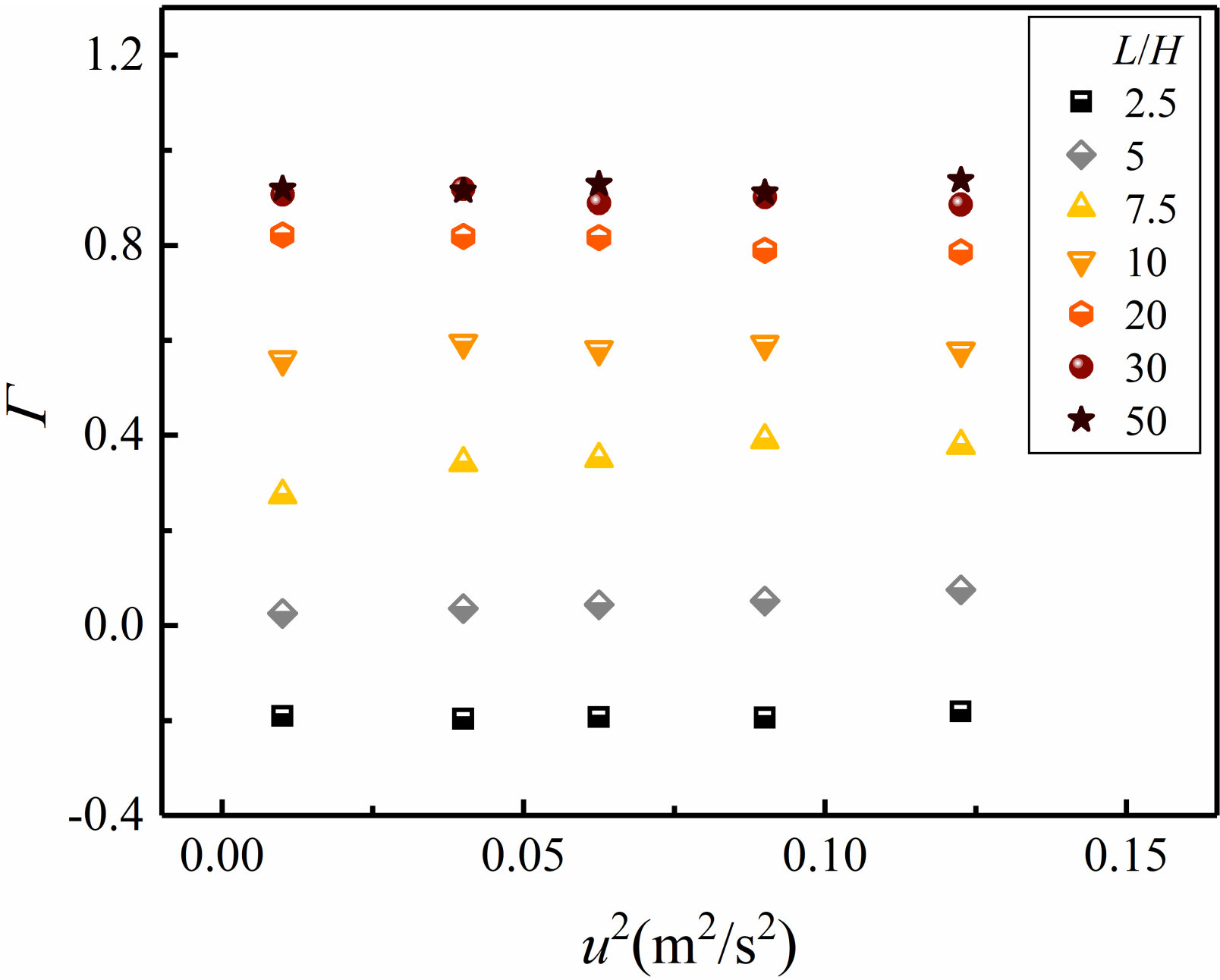
1.2
0.8
0.4
0.0
-0.4
Γ
0.00
0.05
0.10
0.15
u²(m²/s²)
L/H
2.5
5
7.5
10
20
30
50

Figure 6.

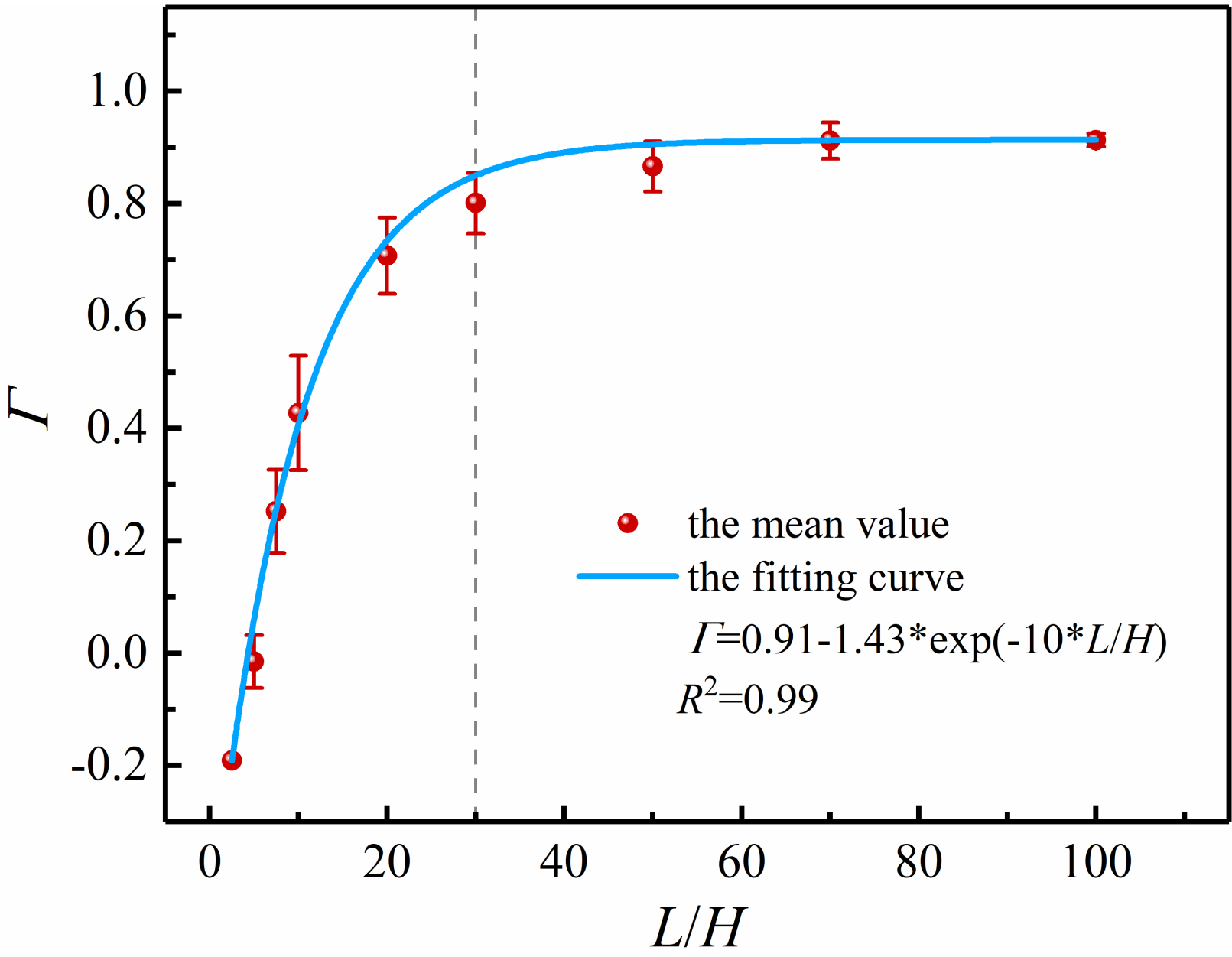
1.0
0.8
0.6
0.4
0.2
0.0
-0.2
Γ
0
20
40
60
80
100
L/H
the mean value
the fitting curve
Γ=0.91-1.43*exp(-10*L/H)
R²=0.99

Figure 7.

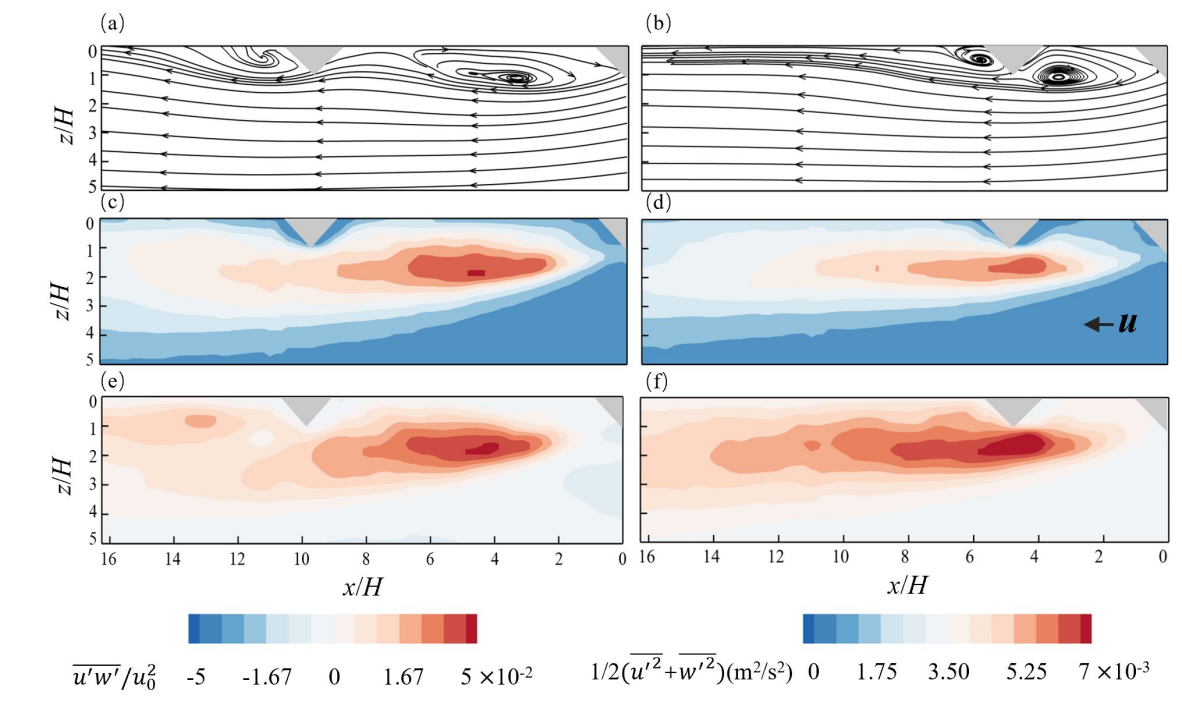
(a)
(b)
(c)
(d)
(e)
(f)
z/H
x/H
0
1
2
3
4
5
16
14
12
10
8
6
4
2
0
u
$\overline{u'w'}/u_0^2$ -5 -1.67 0 1.67 5 ×10-2
$1/2(\overline{u'^2}+\overline{w'^2})$(m²/s²) 0 1.75 3.50 5.25 7 ×10-3

Figure 8.

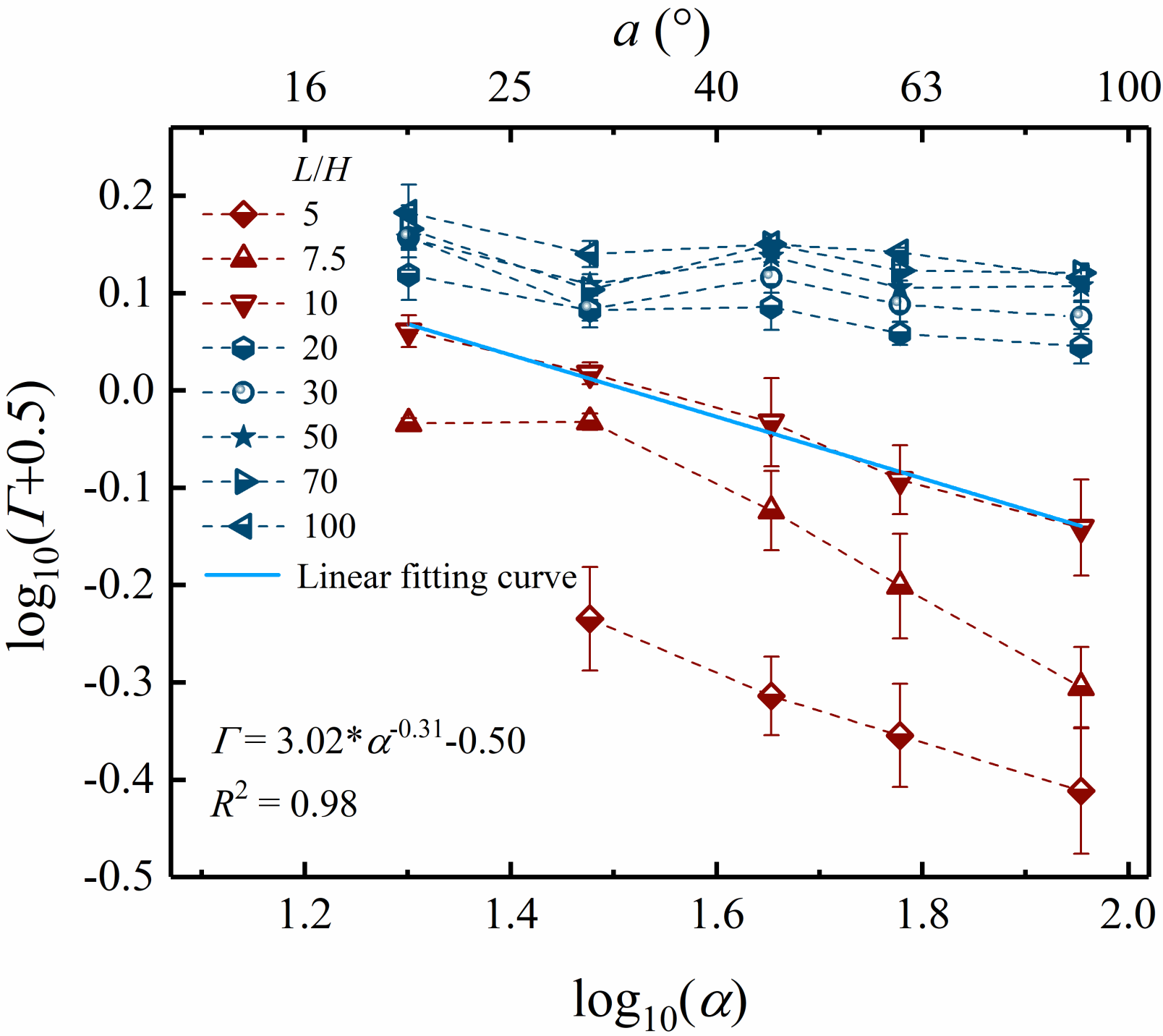
a (°)
16
25
40
63
100
L/H
5
7.5
10
20
30
50
70
100
Linear fitting curve
Γ= 3.02*α^-0.31-0.50
R^2 = 0.98
log10(Γ+0.5)
log10(α)
0.2
0.1
0.0
-0.1
-0.2
-0.3
-0.4
-0.5
1.2
1.4
1.6
1.8
2.0

Figure 9.

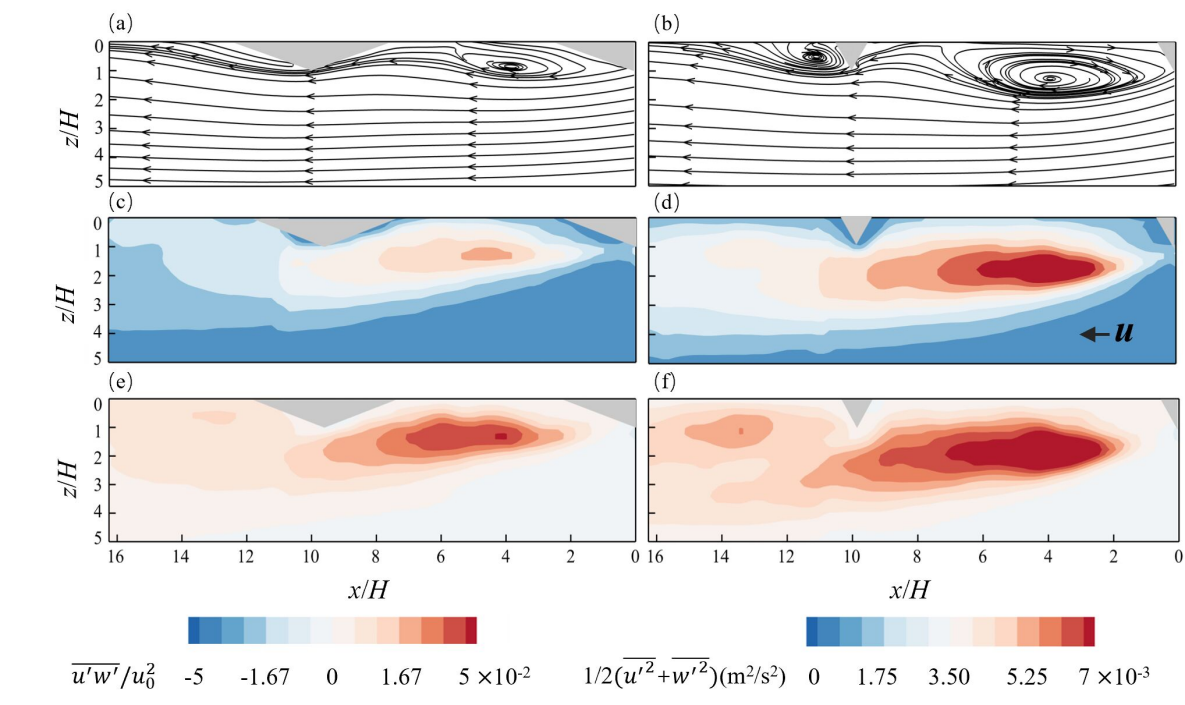
(a)
(b)
(c)
(d)
(e)
(f)
z/H
x/H
0
1
2
3
4
5
16
14
12
10
8
6
4
2
0
←u
$\overline{u'w'}/u_0^2$ -5 -1.67 0 1.67 5 ×10-2
$1/2(\overline{u'^2}+\overline{w'^2})$(m²/s²) 0 1.75 3.50 5.25 7 ×10-3

Figure 10.

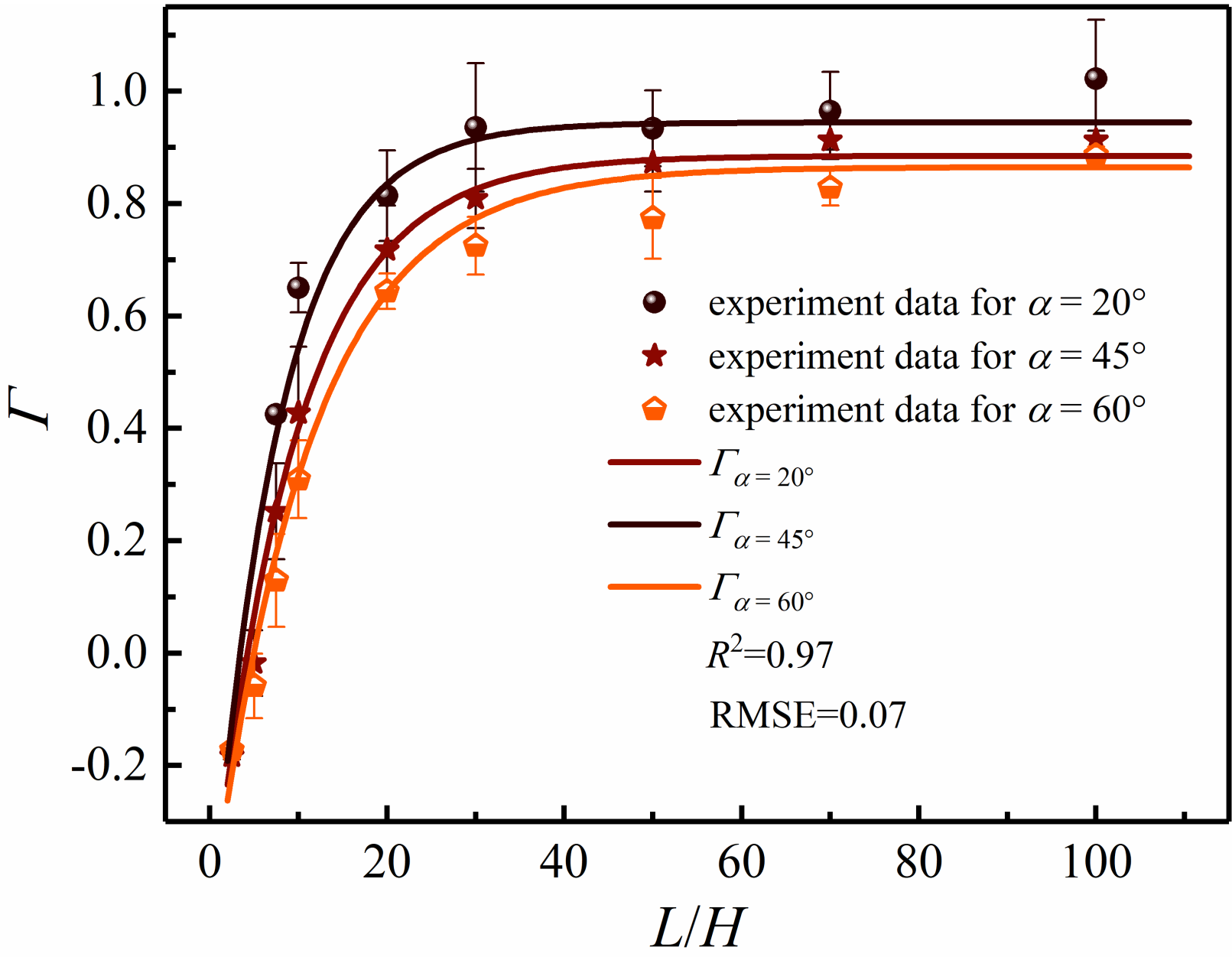
1.0
0.8
0.6
0.4
0.2
0.0
-0.2
Γ
0
20
40
60
80
100
L/H
experiment data for α = 20°
experiment data for α = 45°
experiment data for α = 60°
Γ α = 20°
Γ α = 45°
Γ α = 60°
R²=0.97
RMSE=0.07

Figure 11.

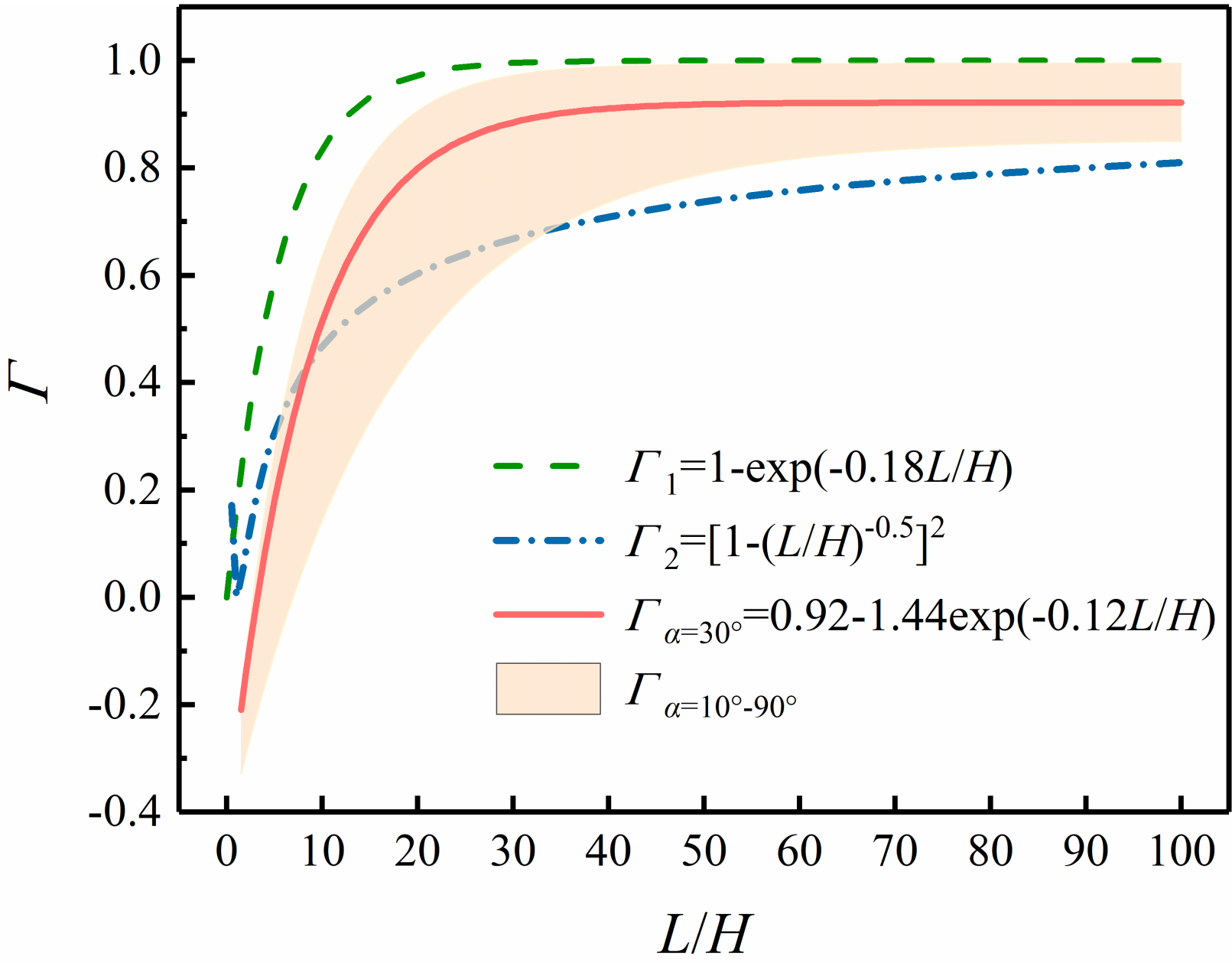
1.0
0.8
0.6
0.4
0.2
0.0
-0.2
-0.4
Γ
0
10
20
30
40
50
60
70
80
90
100
L/H
Γ1=1-exp(-0.18L/H)
Γ2=[1-(L/H)-0.5]2
Γα=30°=0.92-1.44exp(-0.12L/H)
Γα=10°-90°

Figure 12.

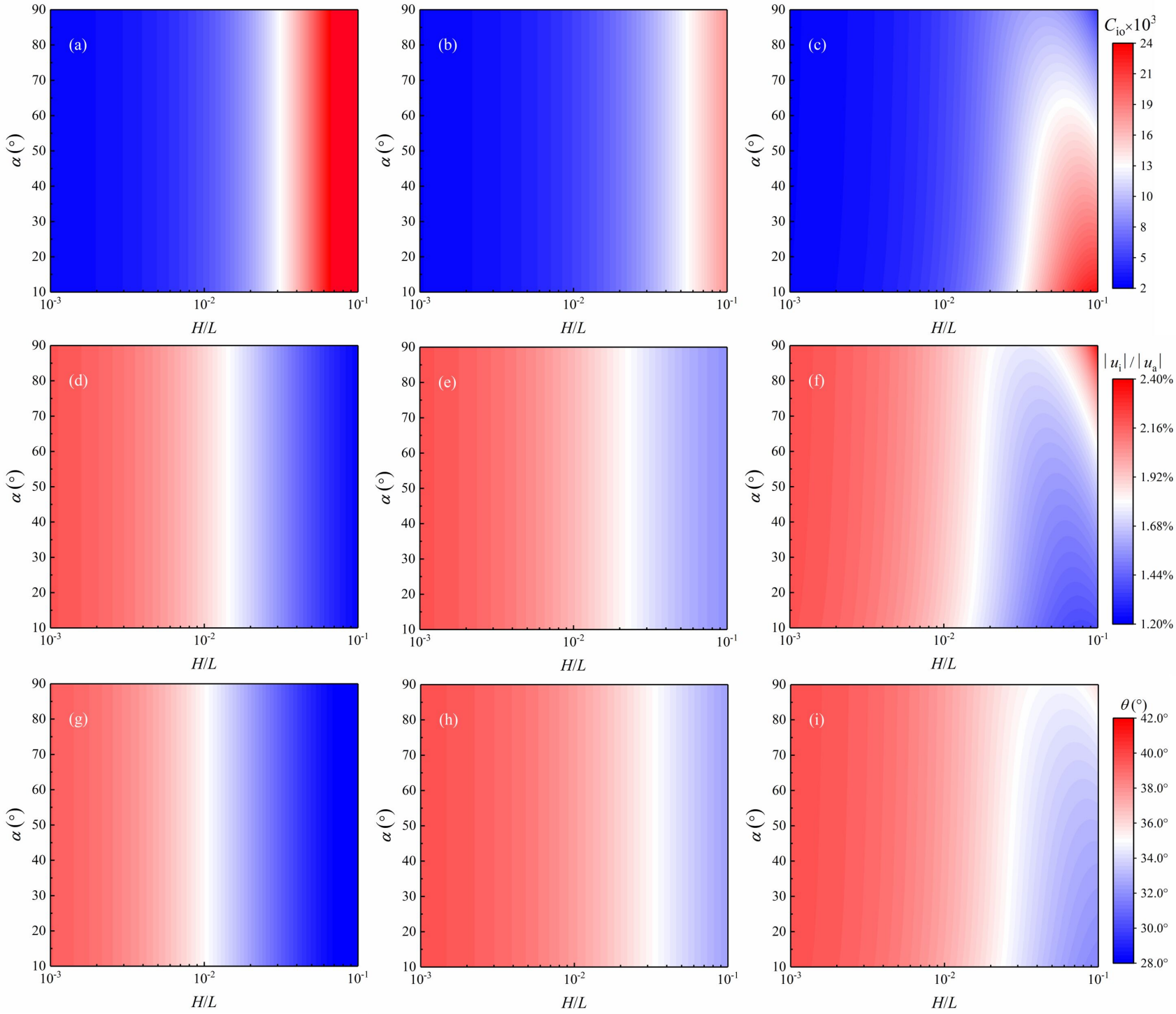
(a)
(b)
(c)
(d)
(e)
(f)
(g)
(h)
(i)
α (°)
H/L
10-3
10-2
10-1
10
20
30
40
50
60
70
80
90
Cio×10³
24
21
19
16
13
10
8
5
2
|ui|/|ua|
2.40%
2.16%
1.92%
1.68%
1.44%
1.20%
θ (°)
42.0°
40.0°
38.0°
36.0°
34.0°
32.0°
30.0°
28.0°

Figure 13.

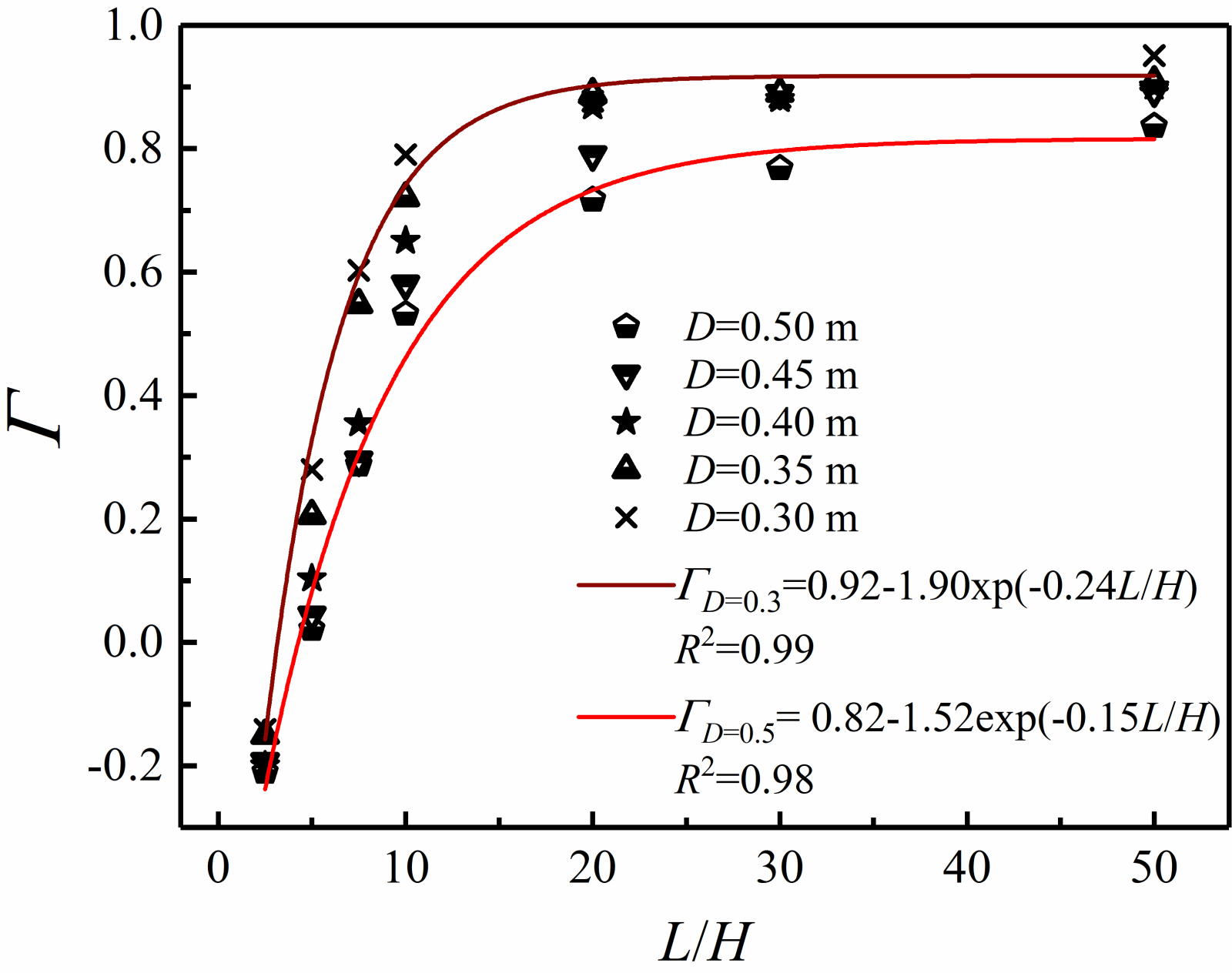
1.0
0.8
0.6
0.4
0.2
0.0
-0.2
Γ
0
10
20
30
40
50
L/H
D=0.50 m
D=0.45 m
D=0.40 m
D=0.35 m
D=0.30 m
Γ D=0.3=0.92-1.90xp(-0.24L/H)
R2=0.99
Γ D=0.5= 0.82-1.52exp(-0.15L/H)
R2=0.98